

Article

Synchronized Full-Field Strain and Temperature Measurements of Commercially Pure Titanium under Tension at Elevated Temperatures and High Strain Rates

Guilherme Corrêa Soares * and Mikko Hokka

Impact—Multiscale Mechanics Research Group, Engineering Materials Science, Materials Science and Environmental Engineering, Tampere University, P.O. Box 589, 33014 Tampere, Finland; mikko.hokka@tuni.fi
* Correspondence: guilherme.correasoares@tuni.fi

Abstract: Understanding the mechanical behavior of materials at extreme conditions, such as high temperatures, high strain rates, and very large strains, is fundamental for applications where these conditions are possible. Although tensile testing has been used to investigate material behavior under high strain rates and elevated temperatures, it disregards the occurrence of localized strains and increasing temperatures during deformation. The objective of this work is to combine synchronized full-field techniques and an electrical resistive heating system to investigate the thermomechanical behavior of commercially pure titanium under tensile loading at high temperatures and high strain rates. An electrical resistive heating system was used to heat dog-bone samples up to 1120 °C, which were then tested with a tensile Split Hopkinson Pressure Bar at strain rates up to 1600 s⁻¹. These tests were monitored by two high-speed optical cameras and an infrared camera to acquire synchronized full-field strain and temperature data. The displacement and strain noise floor, and the stereo reconstruction error increased with temperature, while the temperature noise floor decreased at elevated temperatures. A substantial decrease in mechanical strength and an increase in ductility were observed with an increase in testing temperature. The localized strains during necking were much higher at elevated temperatures, while adiabatic heating was much lower or non-existent at elevated temperatures.

Keywords: high temperature; digital image correlation; infrared thermography; full-field measurements; commercially pure titanium; high strain rate; split Hopkinson pressure bar



Citation: Soares, G.C.; Hokka, M. Synchronized Full-Field Strain and Temperature Measurements of Commercially Pure Titanium under Tension at Elevated Temperatures and High Strain Rates. *Metals* **2022**, *12*, 25. <https://doi.org/10.3390/met12010025>

Academic Editor: Ezio Cadoni

Received: 22 November 2021

Accepted: 20 December 2021

Published: 23 December 2021

Publisher's Note: MDPI stays neutral with regard to jurisdictional claims in published maps and institutional affiliations.



Copyright: © 2021 by the authors. Licensee MDPI, Basel, Switzerland. This article is an open access article distributed under the terms and conditions of the Creative Commons Attribution (CC BY) license (<https://creativecommons.org/licenses/by/4.0/>).

1. Introduction

Titanium alloys are consistently employed in aerospace and racing engineering applications, due to their high mechanical resistance and low density. These engineering parts and components can reach high temperatures (e.g., during atmospheric reentry) and experience dynamic events (e.g., bird ingestion into an airplane turbine). Therefore, there is a demand to investigate the mechanical behavior of these alloys under such extreme conditions. Most investigations on the high-temperature dynamic response of titanium alloys have been conducted on the Ti6Al4V in compression [1–5], and fewer studies have addressed its tensile [6] and shear [7] responses. Regardless of the loading mode, performing high-temperature dynamic tests is not simple, as the specimen needs to be heated up to high temperatures while also keeping heat diffusion to the testing setup as low as possible. A temperature gradient in the Split Hopkinson Pressure Bar (SHPB) distorts elastic wave propagation, changes the particle velocity, and causes additional dispersion to the loading pulses [8]. These factors interfere with the precision of the stress and strain measurements made during mechanical testing. Hueto et al. [6] compared the dynamic behavior of Ti6Al4V in tension with a furnace heating and an electrical resistive heating system. One of the issues with the furnace heating in their investigation, was that the thermal expansion caused by the high-temperature system on the bars and fixtures caused considerable noise

on the measured loading pulses. The results from the electrical resistive heating system were less noisy, as the rapid heating allowed for the sample to be tested before noticeable heat was transferred to the bars. Regular tensile testing provides information on the general mechanical behavior of the material at high strain rates and elevated temperatures, but provides only single average stress and strain values for a given timestamp during the test. However, there is more to a tensile test than what a single average value over the gauge volume can describe, as materials can display strain localization and localized adiabatic heating in phenomena such as necking [6], shear bands [2,5], and Portevin–Le Chatelier (PLC) bands [9]. For this reason, it is interesting to pursue the acquisition of full-field measurements during testing so that such phenomena can be properly described and investigated.

Measuring full-field strains at high temperatures comes with its own challenges, such as dealing with the incandescence, the need for an elastic and temperature-resistant pattern, and the use of a relatively rapid heating system. Hueto et al. [6] reported that furnace heating excessively dried up the heat-resistant paint, making it inadequate for Digital Image Correlation (DIC) analysis. However, the speed of the electrical resistive heating system allowed the paint to remain elastic and follow the deformation, even during necking. The authors were able to monitor the evolution of localized strains throughout the gage length of the tensile sample at 700 °C and a strain rate of 1300 s⁻¹. Pan et al. [10] used an infrared heating device to heat up a stainless steel sample up to 1200 °C, and measured full-field thermal deformation with DIC. In their study, a bandpass filter (428–470 nm) was used to filter out any emitted radiation in the visible range, and a mixture of cobalt oxide and a high-temperature inorganic adhesive was used to make a temperature-resistant pattern for DIC. Novak and Zok [11] performed full-field strain measurements on a Ni-based superalloy and a C/SiC composite and used a laser heating system to heat samples up to 1500 °C. The authors used a bandpass filter (430–500 nm) to limit the wavelength of emitted light, an air knife to decrease the effect of heat haze, and alumina or zirconia paints for DIC speckling. Wang et al. [12] were able to perform DIC and measure full-field strains in tension at a strain rate of 6 × 10⁻⁴ s⁻¹ and temperatures up to 2000 °C by combining electric heating technology with a blue light bandpass filter and an alumina paint temperature-resistant speckle pattern. In their study, the bandpass filter (425–475 nm) was effective in weakening thermal radiation while allowing visualization of the patterned surface. Guo et al. [13] used plasma spray to prepare a tungsten pattern which allowed DIC to be performed during tensile tests at temperatures up to 2600 °C. In this study, the authors combined a bandpass filter (445–455 nm), with a linear polarizing filter and neutral density filters to address incandescence. Valeri et al. [14] investigated the tensile response of a metastable 304 stainless steel at strain rates from 5 × 10⁻⁴ to 10⁻¹ s⁻¹ and temperatures up to 900 °C by combining DIC and Virtual Fields Method. The authors used an induction heating device that required several minutes to achieve uniformity at the target temperature and a DIC pattern produced by a combination of a high-temperature-resistant white yttrium spray paint background and black silica based ceramic paint speckles. In their study, a blue bandpass filter (425–495 nm) was used to mitigate the effect of incandescence on the strain measurements. Pan et al. [15] used 3D-DIC to measure the full-field strains caused by thermal expansion in tungsten at temperatures above 3000 °C. To perform measurements at these ultra-high temperatures, the authors used tantalum carbide for patterning, and addressed the incandescence with a combination of band filters (420–455 and 405–435 nm) and blue self-radiating lights.

The most common methods for measuring temperatures during mechanical testing are thermocouples, infrared detectors, and infrared imaging. Although the use of multiple infrared detectors in parallel allows the acquisition of crude maps [16–18], it is realistic to say that infrared imaging is the only technique which allows for full-field temperature measurements. Orteu et al. [19] developed a method for measuring both full-field strains and temperatures that used a calibrated and uncooled charge-coupled-device (CCD) camera. They were able to measure radiometric temperatures based on the near-infrared

spectral band and were able to make accurate measurements of an object from 300 up to 1000 °C. Tang et al. [20] proposed an optical method based on the red and blue radiation and reflected light to measure temperatures from 500 to 1000 °C of flame-heated specimens. Cholewa et al. [21] used infrared thermography (IRT) to measure full-field temperatures of E-glass/vinyl ester/balsa sandwich composites under compression with one-sided heating. The authors observed temperatures up to 120 °C during their tests and calibrated their infrared camera to handle temperatures up to 500 °C. Although several studies have used IRT to investigate material behavior [22–29], these studies have mostly been performed at temperatures near room temperature, and have not dealt with high temperatures. Soares et al. [27] reported a temperature rise of 80 °C in CoCrFeMnNi alloy under compression at a strain rate of 1 s^{-1} and 0.5 strain, whereas Vazquez-Fernandez et al. [26] observed temperatures up to 100 °C during the uniform deformation of a metastable stainless steel specimens in tension at a strain rate of 10 s^{-1} . Smith et al. [23] observed a temperature increase of 150 °C during necking of Ti6Al4V alloy specimens in tension at 2000 s^{-1} . Tarfoui et al. [29] investigated heat dissipation in E-glass/Epoxy laminated composites under dynamic compression and observed a maximum temperature that exceeded 219 °C. Seidt et al. [24] measured temperatures of roughly 370 °C during necking of a stable austenitic stainless steel specimen tested in tension at strain rates of 200 and 3000 s^{-1} . To properly carry out these measurements at such temperatures, the authors had to adjust the camera integration time from 10 to 5 μs , so that the infrared detector would not saturate during the test. Nie et al. [28] reported temperatures up to 497 °C in their work on the formation of adiabatic shear bands in aluminum alloys on flat hat-shaped specimens tested with a modified compression SHPB setup. The low emissivity of the investigated alloys, of approximately 0.15, allowed them to make measurements up to such temperatures without the use of any attenuation filters. Shen et al. [30] and Liu et al. [31] used a HgCdTe infrared detector to monitor the temperature of shape memory and pseudoelastic NiTi alloys under high strain rate compression and reported different maximum temperatures and temperature variations during loading and unloading. To the best of the authors' knowledge, there has not been any full-field temperature measurements of materials tested at very high temperatures, especially at high strain rate tensions. Furthermore, to fully utilize these full-field measurements to characterize material behavior, it is essential to integrate them in a single and robust thermomechanical analysis.

The combination of synchronized full-field strain and temperature measurements can be a robust tool for engineers and material scientists, as it provides vast amounts of data on the thermomechanical behavior of the materials. The data acquired from such an integration can be used to validate and improve material models, investigate material failures, and to perform fundamental research on the microstructural evolution of materials. Previous research has already demonstrated the various benefits and potentials of such measurements. Orteu et al. [19] performed full-field strain and temperature measurements with uncooled CCD cameras by combining DIC and full-field temperature measurements with a radiometric calibration. Using only a single camera for both measurements, the authors demonstrated that a simplified method with an inherent spatial correspondence could be also applied to higher-speed CCD cameras. Nevertheless, to perform near-infrared temperature measurements with CCD cameras requires the target material to be at least at 300 °C. Tang et al. [20] also proposed a single-camera method for measuring both the full-field strains and temperatures of specimens at high temperatures. The authors presented an iterative algorithm based on analyzing the shift of red and green radiation to calculate temperature, while using the blue radiation to measure strains with DIC. In a later work, Tang et al. [32] demonstrated how high-frequency flashing could be used to increase the accuracy of synchronous full-field measurements. The authors proposed that pictures could be taken alternately with and without a flash, so that the pictures for calculating strain are well illuminated while the pictures for calculating temperature are not affected by light reflections. These measurements can then be interpolated and represented synchronously. Chrysochoos et al. [22] brought attention to the many applications where combined DIC

and IRT could offer several benefits for investigating the thermomechanical behavior of materials. Crump and Dulieu-Barton [33] coupled high-speed optical cameras and a medium-speed infrared camera (up to 20 kHz) to investigate the development of the shape and temperature of a steel specimen under tensile loading at different strain rates. Seidt et al. [24] and Gilat et al. [25] integrated high-speed optical and infrared cameras to perform full-field strain and temperature measurements in an austenitic stainless steel specimens deforming under tensile loads at strain rates between 10^{-2} and 3000 s^{-1} . Smith et al. [23] further developed the integration of the measurements as they investigated the full-field deformation and temperature evolution in Ti6Al4V specimens in tension from 1 to 7000 s^{-1} . To represent the full-field data of their studies, these authors used 2D waterfall plots of axial strain and temperature as a function of position through the gage length and time. Cholewa et al. [21] combined their full-field temperature measurements with full-field strain measurements in their investigation on the compressive loading of sandwich composites. The main motivation for their work was the development of an integrated technique, which would be applicable for different length scales. In their work, the authors only imaged one surface of the sample, and had to combine the use of a paint with a known emissivity for IRT with a paint with a negligible effect on IRT for the DIC pattern. Despite these efforts, the synchronized deformation and temperature measurements during high-speed testing, the majority of work has been limited to testing at temperatures close to room temperature.

High-temperature dynamic tensile testing [6] and low-temperature synchronized full-field strain and temperature measurements in dynamic tension [23] have already been successfully performed. However, there has not yet been any report of a full-field study of a tension test at a high strain rate and elevated temperatures. The novelty and relevance of this work are the synchronized full-field strain and temperature measurements of commercially pure titanium in dynamic tension loading at elevated temperatures, the detailed description of the difficulties and their solutions that occurred while carrying out the measurements, and the assessment of the measurement uncertainties especially at elevated temperatures. The method can be used for various applications where high strain rates and elevated temperatures occur simultaneously. In addition to the description of the method, we show results obtained for commercially pure titanium in tension at high strain rates and elevated temperatures. We discuss also how this method can provide data that further improves the current understanding of the relationship between strain localizations and adiabatic heating under a high strain rate and high-temperature conditions, as well as improve current material modelling and simulations of high-temperature applications.

2. Materials and Methods

2.1. Material

The investigated material was commercially pure titanium, which was received as a thin sheet in annealed condition. Samples were cut by electrical discharge machining with a special dog-bone geometry designed for the high-temperature tests. The specimen dimensions and geometry are shown in Figure 1 and Table 1. The vertical protuberances on the sample are necessary for the electrically resistive electric system to run an electric current through the gage length of the sample. To ensure the contact of the electrically resistive heating system, these protuberances were ground with a 1200-grit sandpaper and were kept clear of any paint or glue throughout the whole testing process. A black temperature-resistant engine manifold spray paint (VHT Paints, Cleveland, OH, USA) was used to pattern one of the sides of the sample in the gage length section to enable DIC. The spray-painted pattern resisted temperatures up to $1120 \text{ }^\circ\text{C}$ but was erased at higher temperatures. The other side of the sample was not painted, and was only ground with a 1200-grit sandpaper and cleaned with ethanol/acetone for infrared imaging. There were other attempts at patterning the sample with different methods, such as with permanent markers and regular spray paints, but the patterns were consistently wiped out at much lower temperatures.

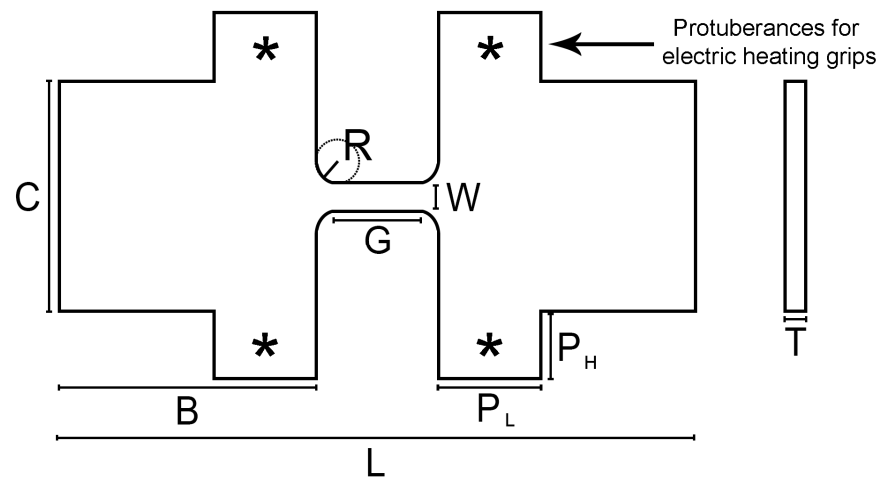


Figure 1. Specimen geometry used for the high-temperature tensile tests in the Split Hopkinson Pressure Bar. The asterisks indicate the protuberances for the electric heating grips.

Table 1. Dimensions of the tensile samples (mm).

G	W	T	B	C	L	P _L	P _H	R
8	4	2	25	22	62	10	7	2

2.2. Experimental Setup

The mechanical tests were performed with a tensile SHPB from room temperature up to 1120 °C at strain rates of approximately 1000 to 1600 s⁻¹. The results of these tests are presented as engineering stress–strain plots in the results section. The SHPB setup consists of a gas gun, a striker tube, a steel incident bar, and an aluminum transmitted bar. The incident and transmitted bars were resting on stanchions with bearings that ensured the alignment and free movement of the bars. The gas gun accelerates the striker tube, which then impacts the end of the incident bar and produces a tension stress pulse, which travels towards the sample. The incident bar and transmitted bars have two 5-mm strain gages attached to their surfaces to measure the incident, transmitted, and reflected pulses. A Kyowa CDF 700 A signal conditioner (Kyowa Electronic Instruments Co., Ltd., Tokyo, Japan) was used to amplify the strain gage signals, which were then recorded on a 12 M Sample digital oscilloscope (Yokogawa Electric, Musashino, Japan). The oscilloscope data acquisition was triggered by a rising edge from the strain gage signal in the incident bar. A numerical dispersion-correction method, based on the work by Gorham and Wu [34], was applied to correct the effects of longitudinal wave dispersion in the loading pulses. A Fast Fourier Transform (FFT) filter with a cut off frequency of 50 kHz was applied to the loading pulses of the tests at elevated temperatures to decrease the electric noise generated by the heating system. The stress, strain, and strain rates were then calculated from the dispersion-corrected and FFT-filtered pulses. A more comprehensive description of the setup, its inner workings, and examples are found in references [35–37].

An electrical resistive heating system was used to heat up the tensile samples just moments before the arrival of the loading pulse. This ensured the least amount of temperature diffusion would occur from the sample to the bars. This system comprises a welding transformer, pneumatic grips with copper spot-welding electrodes, and a custom-made controller integrated with the SHPB system. It relies on the Joule heating to heat up only the gage section of the tensile sample, as the pneumatic grip grabs the protuberances from the specimen and the welding transformer passes a high-ampereage–low-voltage direct current (DC) from one protuberance to the other. One of the main advantages of this system over more traditional furnace and induction systems is the short time necessary to heat up the specimen to high temperatures. The heating of the sample in less than a second

offers less time for the surface to oxidize and for the painted pattern to break, enabling DIC at high temperatures. To ensure that the current would only run through the sample, the bars and stanchions were electrically isolated using rubber pads under the stanchions and insulation tape in the places where the bars contacted the stanchions. The control of the heating system is integrated with that of the SHPB so that the sample is quickly heated up and the pneumatic clamps disengage just moments before the incident pulse arrives at the sample interface. This automated procedure minimizes the amount of heat transferred from the sample to the bars, mitigating any negative effects that would arise from having a temperature gradient affect the bars' mechanical properties. Furthermore, the rapid heating allows the specimen to be fixed to the bars by a cyanoacrylate superglue, instead of using mechanical clamping, threads, pins, or similar measures, which often disturb the motion of the stress waves, causing unwanted oscillations to the stress pulses [6]. A more detailed description of this electrical resistive electric heating system and a comparison to a more conventional furnace heating system can be found in the work of Hueto et al. [6].

2.3. Optical and Infrared Imaging at Elevated Temperatures

The mechanical tests were monitored by two Photron Fastcam SA-X2 high-speed cameras (Photron, Tokyo, Japan) with 100-mm lenses and a Telops Fast-IR 2 K high-speed infrared camera (Telops, Quebec City, Canada) with a 50-mm lens. The optical cameras imaged the patterned side of sample, while the infrared camera imaged the clean side of the sample through a hole in the aluminum plate supporting the pneumatic clamps. The tensile sample was illuminated by Ultra-Bright cold LED modules. The complete experimental setup is shown in Figure 2.

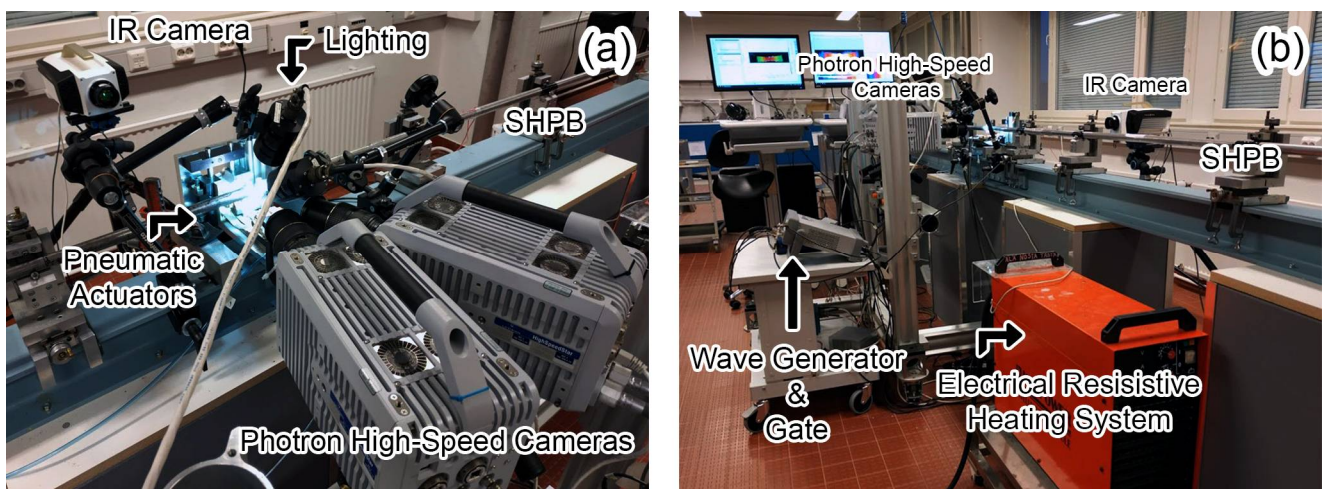


Figure 2. Experimental setup for the high-temperature and high-strain rate tensile tests. (a) Close-up showing the cameras, lighting, and pneumatic actuators for the heating system, and (b) general view also showing the electrical resistive heating system, the wave generator, and the analog gate.

2.3.1. High-Speed Optical Imaging

Although matter emits electromagnetic radiation at any given temperature, it is usually in the infrared range and does not affect optical imaging. However, this emitted radiation shifts to lower wavelengths with an increase in temperature and reaches the visible spectrum at the Draper point of 525 °C. The intensity of the radiation emitted by an object is therefore a function of its temperature and wavelength, and can be evaluated by its spectral radiance, L . The emission of visible radiation influences the gray levels observed by optical cameras and needs to be considered when acquiring optical images of incandescent objects. This becomes important for the DIC measurements, which are based on the variation of gray levels in a pattern. To address the effects of incandescence on the optical images, it is essential to understand the wavelength and intensity that are

being emitted at a given temperature range where the measurements are carried out. The spectral radiance per unit of wavelength of a perfect black body can be described by Planck's radiation law expressed in terms of wavelength, which is shown in Equation (1), where λ , T , h , c , and k_B , respectively, represent the wavelength, temperature, Planck constant, speed of light, and Boltzmann constant.

$$L(\lambda, T) = \frac{2hc^2}{\lambda^5} \frac{1}{e^{\frac{hc}{\lambda k_B T}} - 1} \quad (1)$$

To properly visualize the patterned sample surface at temperatures above 525 °C, it is necessary to filter the radiation emitted in the visible spectrum. Equation (1) allows for the visualization of what radiation would be emitted by matter as a function of temperature, and the analysis of the radiation range expected in our tests led to the choice of using a blue-green shortpass filter (410–570 nm, SP570, Midwest Optical Systems, Palatine, IL, USA) with the optical cameras used in this study. Figure 3 shows the temperature and wavelength dependence of the spectral radiance, the shortpass filter cut-off wavelengths, and the associated transmission. The intensity of visible radiation in the red and orange range increases rapidly at temperatures above 800 °C, which led to the choice of a filter that would cut these wavelength components off from the optical images. It is noteworthy that the filter used in this work allowed for a wider range of wavelengths to pass than in other high-temperature DIC studies [11,12,14] and the reason for that is the high-speed nature of the tests and the short exposure times needed for this work. From Figure 3b, one can conclude that the filter that was used was adequate, and that it filtered out most of the incandescent radiation up to 1100 °C, and still filtered a lot of the radiation at 1200 °C. This visible radiation, which influences the optical images at temperatures above 1100 °C, are certainly a source of uncertainty in the DIC measurements.

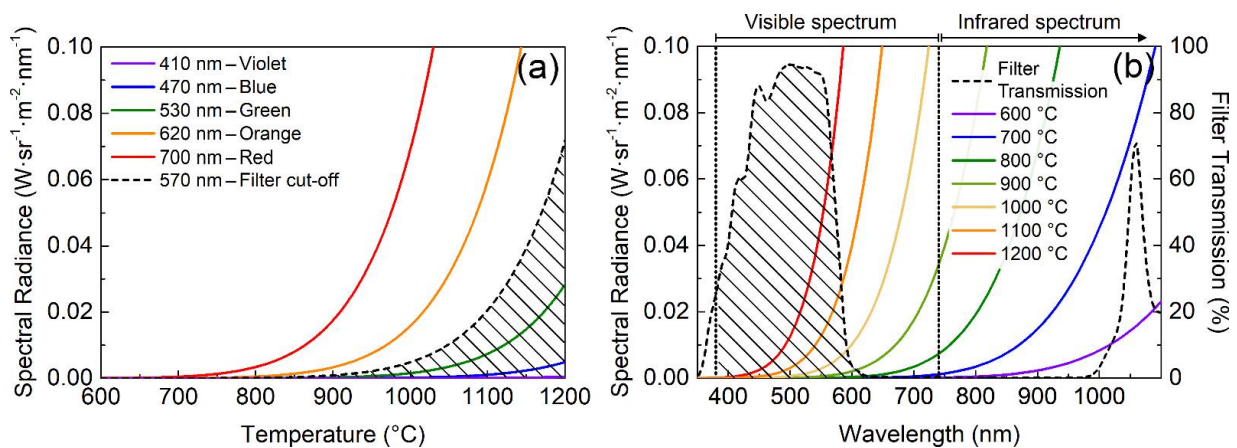


Figure 3. (a) Spectral radiance as a function of temperature for different wavelengths. The hatched area under the dashed line shows the radiation that passes through the shortpass filter and (b) the spectral radiance (solid lines) and the blue-green shortpass filter transmission (dashed line) as a function of wavelength for different temperatures. The hatched area under the dashed line shows the wavelength range in the visible spectrum, which passes through the filter.

Figure 4 shows optical images obtained with and without the shortpass filter at room temperature and at 950 °C of a specimen, where half of the gage length was spray-painted. The surface of the specimen is only visible at high temperatures if the shortpass filter is used. Although the filter does reduce the amount of light captured at room temperature, the LED lights still provide enough light for the sample surface to be properly imaged.

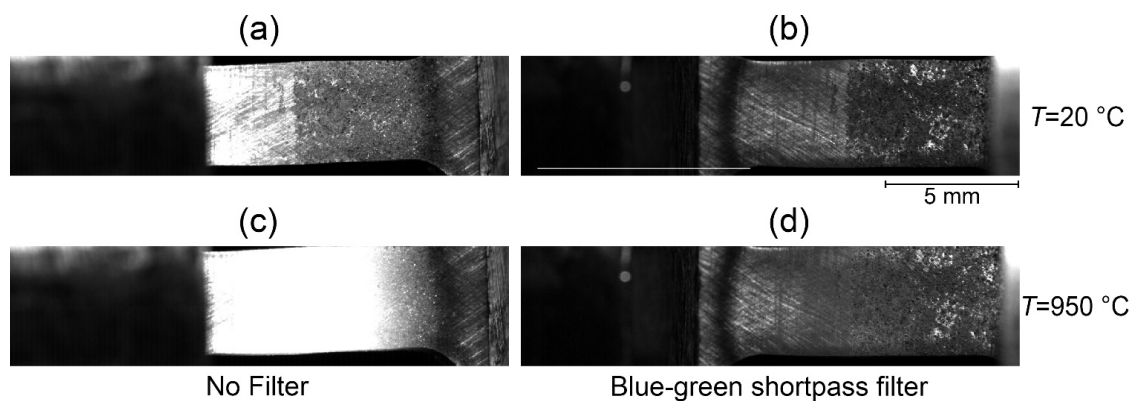


Figure 4. Optical images of a tensile sample at room temperature (a,b) and at $950\text{ }^{\circ}\text{C}$ (c,d) imaged without a filter (a,c) and with a blue-green shortpass filter (b,d). The left side of the sample had a ground surface while the right side of the sample was patterned with a high-temperature spray paint. The bright hatched marks on the left side of the specimen are specular reflections from the ground surface.

Figure 5 shows the surface of a specimen prior to heating at room temperature and at a temperature of $880\text{ }^{\circ}\text{C}$. While the pattern is still clearly visible at the high temperature, it has less contrast than at room temperature. The average intensity of the pattern was measured at both temperatures, and the standard deviation at high temperatures was 50% lower than that at room temperature, showing that the high-temperature image has approximately only half of the gray value range of the image at room temperature. Despite a higher contrast being normally preferred, the contrast was sufficient for the DIC analysis at elevated temperatures.

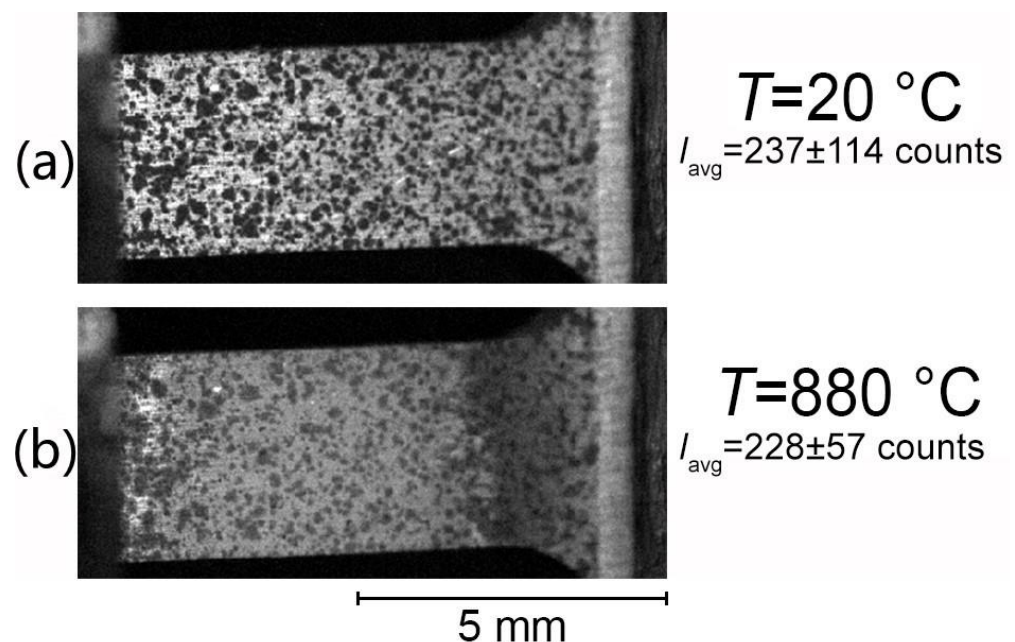


Figure 5. Optical images of spray-painted pattern at (a) room temperature and at (b) $880\text{ }^{\circ}\text{C}$. I_{avg} is the average light intensity from the specimen's gauge length and the standard deviation is an indication of the contrast at a given condition (a bigger standard deviation indicates more levels of gray between black and white). These pictures were taken using the blue-green shortpass filter.

2.3.2. High-Speed Infrared Imaging

The infrared camera has a filter wheel that allows for imaging at different temperature ranges without reaching sensor saturation. An attenuation filter calibrated for radiometric temperatures from 249 to 1133 °C was used in this investigation. The use of the filter led to challenges in the aiming and focusing of the infrared camera, as turning the filter wheel changes the optical characteristics of the system. The challenge of aiming and focusing the camera with the attenuation filter was overcome by initially performing this procedure at room temperature and using a hot object, such as a soldering iron, to aim and focus with the attenuation filter in place. The image was focused by visualizing sharp edges and the lack of blurry rings around the imaged objects. The change in focus after applying the filter could be such that it would not be possible to focus on the same object without having to physically move the camera. To address this issue, the infrared camera was mounted on a focusing rail, which allowed for the precise movement of the camera without having to move the camera tripod. Figure 6 shows examples of the obtained temperature data and the uniformity of the temperature distribution in a specimen during the tension test.

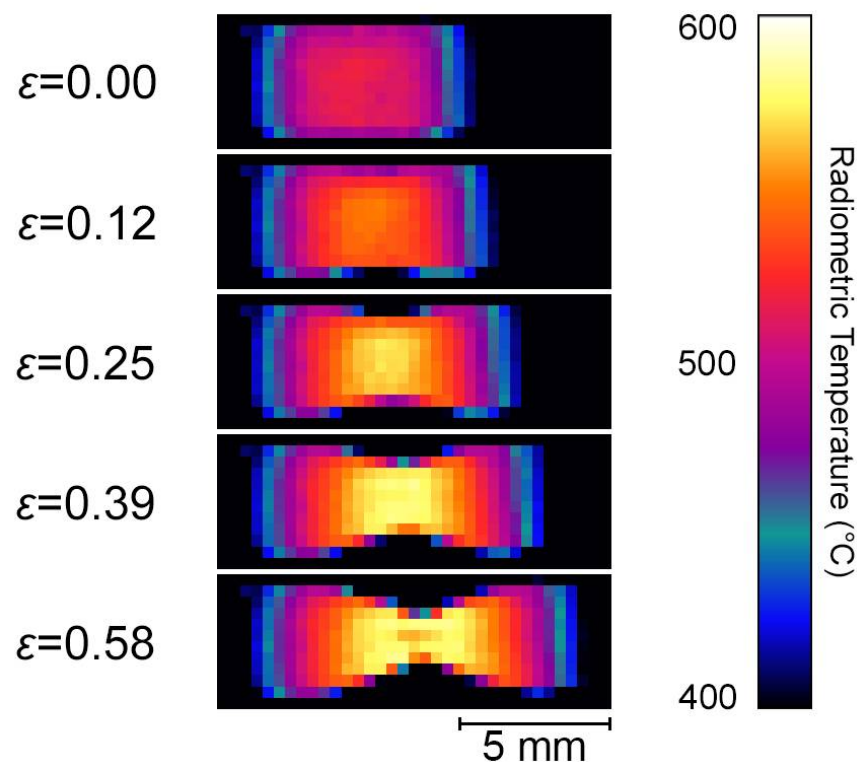


Figure 6. Full-field radiometric temperature evolution caused by adiabatic heating in a commercially pure titanium specimen deformed in tension at strain rate of 1600 s^{-1} at different levels of engineering strain.

2.4. Temporal Synchronization of Data Acquisition

Image acquisition of the optical and infrared cameras was synchronized by triggering them with a Keysight 33,500 B function generator (Keysight Technologies, Santa Rosa, CA, USA). The acquisition frequency on both systems was 62 kHz, the resolution on the optical cameras was of 708×208 pixels, and the resolution of the infrared camera was of 64×16 pixels. Although a higher acquisition rate of 90 kHz could have been used, it would have come at the cost of a considerable resolution trade-off (64×4 pixels). The advantages of having a four-times higher spatial resolution outweighed the disadvantages of using a lower acquisition rate for the current experiments. The function generator produces Transistor–Transistor Logic (TTL) pulses at the desired frequency to clock the Photron cameras and to trigger each image acquisition instance in the infrared camera. The wave

generator produced TTL pulses that had a 5 V amplitude, a 1 μ s pulse width, and an 8.4 ns lead and trail edge. An analog gate was used to block the TTL pulses from reaching the infrared camera before the moment of interest. The activation and timing of the electric heating system was automatically controlled by the Hopkinson Bar device software. The shooting of the striker was automated so that the loading pulse would reach the sample after the heating system had fully heated the specimen up and the pneumatic clamps had disengaged from the specimen. When the oscilloscope begins acquiring data, it sends a trigger signal that both initiates image acquisition in the Photron cameras and opens the gate so that the infrared camera can also start acquiring images. A more detailed description of this synchronization method can be found in ref. [38]. The schematics of this system and the sequence of events during the high strain rate, high-temperature experiments are shown in Figure 7. To ensure the synchronization of the image acquisition in all systems, the trigger-out signals from both the optical and infrared cameras were recorded on the same oscilloscope as the loading pulses from the SHPB. Figure 8 shows the signals for the oscilloscope trigger, wave generator signals, and trigger-out signals from both the optical and infrared systems. The overlapping trigger-out signals from both optical and infrared cameras show the synchronicity of image acquisition and identical exposure time.

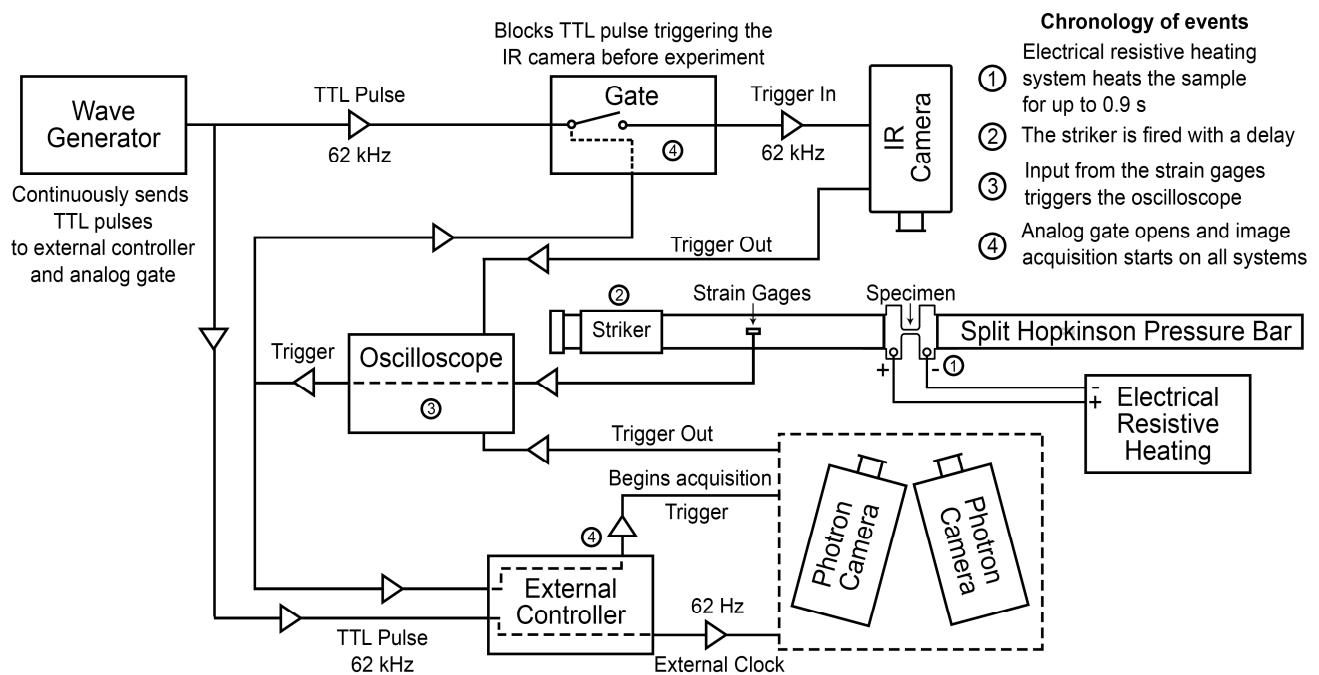


Figure 7. Schematic picture of the testing setup comprising the electrical resistive electric heating system, high-speed cameras, the SHPB tensile bar, the wave generator, the external camera controller, and the path of signals used to synchronously acquire data during the test. The sequence of the events is described in the upper-right corner of the figure and marked with the respective numbers on the picture.

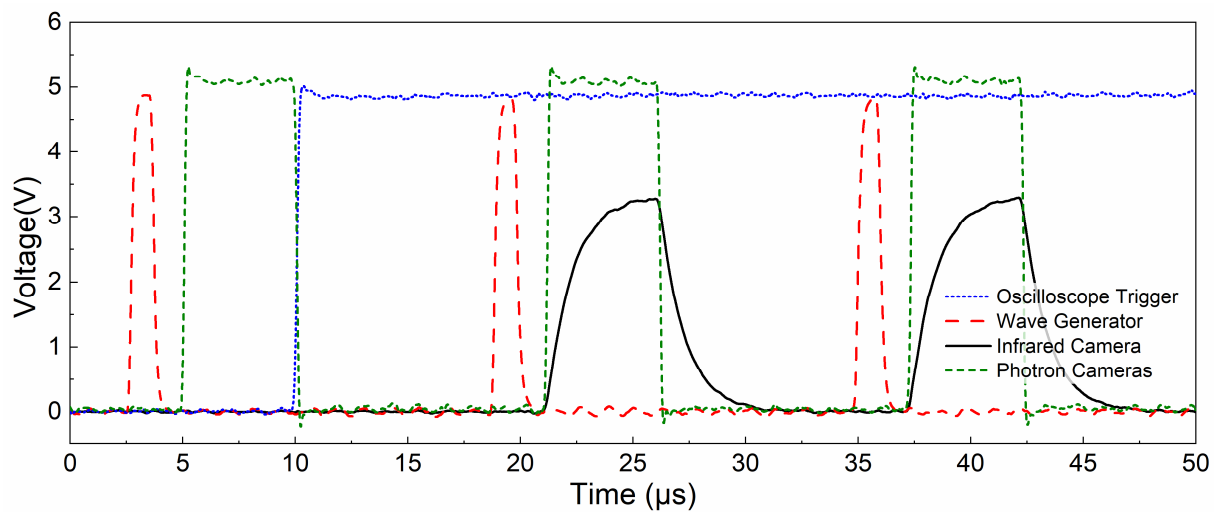


Figure 8. Oscilloscope trigger, wave generator signal, infrared, and optical camera trigger-out signals as a function of time at the moment of the trigger event. The overlapping of the infrared and Photron camera signals show the synchronization of image acquisition after the oscilloscope sends its trigger signal.

2.5. Spatial Calibration of the Systems

A pinhole camera model was calibrated using a set of pictures of a two-level double-sided calibration plate obtained with the high-speed optical and infrared cameras. The calibration plate was positioned between the incident and transmitted bars and imaged as it was rotated and translated to increase the pinhole model accuracy. The usage of the attenuation filter in the infrared camera changes the optical characteristics of the system, so it was necessary to image the calibration plate while still having the attenuation filter on. A heating ring and a longer exposure time were used to attain sharp images with uniform lighting throughout the calibration plate. The setup of the calibration plate with the heating ring and an infrared image of the setup are shown in Figure 9. During this procedure, the calibration plate would generally heat up by maximum of 10 °C due to the heat radiating from the heating ring. This slight increase in temperature should not be an issue, as the manufacturer states that the calibration plate can be used at temperatures from 0 to 40 °C [39]. Furthermore, the calibration plate is made of an AlMnMg alloy, and it would have only shown a linear expansion of approximately 0.024% in the scenario where it was heated by 10 °C.

A spatial calibration procedure was used to calibrate both the intrinsic parameters of each individual camera (e.g., image center, lens focal length, lens distortion, and physical scale) and extrinsic parameters of the system (e.g., stereo angle and distance between the cameras). The full-field strain and temperature evolution of the sample was analyzed with stereo DIC and IRT. Strain and temperature were considered to be equal on both sides of the specimen, since they were cut out from a thin sheet. The incremental correlation mode was used to ensure DIC would be able to follow the deformation of the sample surface, even throughout necking, in tests at elevated temperatures. Although the incremental correlation mode leads to higher uncertainties, the single reference image correlation mode was unable to follow the deformation after the onset of necking or after any changes in the surface roughness during plastic deformation. Therefore, the single reference image correlation mode was only used for the room-temperature tests. For further information on DIC correlation modes and different approaches to define a reference image, the reader is referred to reference [40]. The stereo DIC parameters are shown in Table 2. The spatial calibration allowed the optical and the infrared images to be represented in the same global coordinate system. The origin of the infrared images in the global coordinate system had to be further adjusted manually to correct the projection errors. Such errors can occur due

to many experimental reasons, such as the back of the sample being 2 mm away from the surface imaged by the optical cameras, the calibration plate $z = 0$ plane not being perfectly aligned with the specimen surface, and the somewhat low resolution of the infrared camera in conjunction with having to image the calibration plate using the reflected infrared radiation.

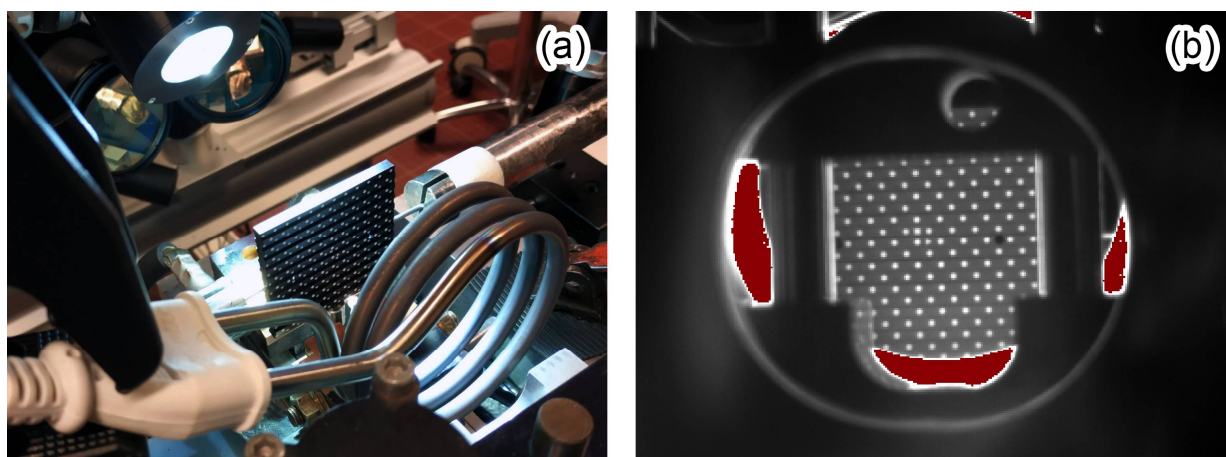


Figure 9. (a) Picture of the two-level double-sided calibration plate used to calibrate the pinhole camera model and the heating ring used to illuminate the calibration plate. (b) Infrared image of the calibration plate illuminated by the heating ring.

Table 2. Stereo Digital Image Correlation parameters.

Sensor and Digitization	1024 × 1024 pixels, 12 bit
Camera Noise (% of range)	1.13–3.50%
Lens and Imaging Distance	100 mm F-mount, 178 mm
Total Number of Images per Test	24–43
Acquisition Frequency (Hz)	62,000
Image Scale Factor (pixel/mm)	40.95–41.39
Region-of-Interest	768 × 255 pixels
Stereo-Angle (°)	27.23–27.76
Matching Criteria	WVSSD *
Interpolant	7-tap B-spline
Subset Shape Function	Affine
Subset Weighting Function	Gaussian
Subset Size (pixel)	45–55
Step Size (pixel)	5
Virtual Strain Gage Size (pixel)	50–60

* Weighted Variables-Based Sum of Squared Differences.

The full-field deformation vectors from DIC are usually represented in a Lagrangian frame of reference, while the full-field temperature maps are represented in an Eulerian frame of reference. What that means is that the spatial or material coordinates of the strain data do not change with time, while the spatial coordinates of the temperature data change with time. To represent both strain and temperature in the same Lagrangian frame of reference, the displacement vectors obtained with DIC were subtracted from the temperature maps to eliminate the shift observed due to the sample movement during deformation. The full-field strain and temperature overlaid maps and 3D waterfall plots presented later in the results section are examples of exploiting the full-field data in the same global coordinate system and frame of reference for comparing the evolution of a deforming specimen during testing. A comprehensive explanation of this procedure and its application to room-temperature tests can be found in reference [38].

2.6. Surface Temperature Calibration

The infrared camera measures radiometric temperature, which assumes that the target object is a black body and has an emissivity of 1 [23]. Considering that most materials are not black bodies, the radiometric temperature is often an underestimation of the real surface temperature value of the target. A calibration from radiometric temperature to surface temperature was performed to address this matter. A K-type thermocouple was spot-welded to the gage section of a tensile samples, which were then heated up to 1400 °C with the electrical resistive heating electric system. The cooling down of the sample was then simultaneously monitored by the thermocouple and the infrared camera. The parameters used for the infrared camera data acquisition (e.g., integration time, camera position in relation to the sample, and acquisition frequency) and the sample preparation were the same as those used during the mechanical testing. The average radiometric temperature of the heated sample was associated to the surface temperature from the thermocouple to construct a calibration curve. To ensure reliability, an average calibration curve was calculated from seven calibration runs.

The response time of the K-type thermocouples was considered adequate for the calibration measurements, despite the thermal inertial effect of the thermocouples, which could have played a role in the measurements due to the rapid cooling rate of the specimen at elevated temperatures. There have been many reports in the literature [41–45] where thermocouples were used successfully to monitor the temperature increase of materials under dynamic loading, which requires a much higher response time than that needed for the calibration measurements in the current work. The uncertainties of the temperature measurements were reduced by carrying out multiple calibration runs to construct the temperature calibration. Performing the calibration by holding the specimen temperature constant for a longer time would certainly allow the thermocouple to reach a thermal equilibrium, but this would also lead to the severe oxidation of the surface and possible changes in the emissivity of the material. The benefits of using a fast thermocouple for monitoring the cooling of the specimen were considered to outweigh the possible disadvantages from the thermal inertial effect.

At radiometric temperatures between 600 and 800 °C, the specimens developed a rougher surface (Figure 10) at the onset of plastic deformation, and an evident drop in radiometric temperature of up to 80 °C was observed. This was associated with the lower emissivity of the rougher surface in comparison to the polished surface at the beginning of the test, and for which the calibrations were carried out. This sharp decrease in average and maximum radiometric temperatures was observed in the raw measurements of several tests and is not an artifact of the custom temperature calibration. This deformation-induced surface roughening is possibly related to heterogeneous out-of-plane movements of the individual grains on the free surface with plastic strain, and it has been previously observed in polycrystalline titanium [46,47]. This phenomenon is often referred to as the “orange peel effect”, and is characterized by the formation of a rougher surface with ridges, valleys, and wavy features [46]. According to Romanova et al. [46], out-of-plane and in-plane grain motion on the free surface led to surface roughening and the formation of surface undulations. The authors also show how roughness of the surface of commercially pure titanium can increase shortly after the beginning of plastic deformation. Such an orange peel pattern formation was not observed at room temperature in the current study, but it was obvious at higher temperatures. It is possible that a thermally activated deformation mechanism, or simply a secondary slip system, e.g., a prismatic or pyramid system, is activated in the hexagonal system above a threshold temperature, which could lead to the observed surface roughening and a decrease in surface emissivity at temperatures above 800 °C. Finally, above 880 °C, the crystal structure of the titanium starts to change from a hexagonal closed-packed to a body-centered cubic structure, which has obvious effects on the grain structure and the plastic deformation of the surface layer.

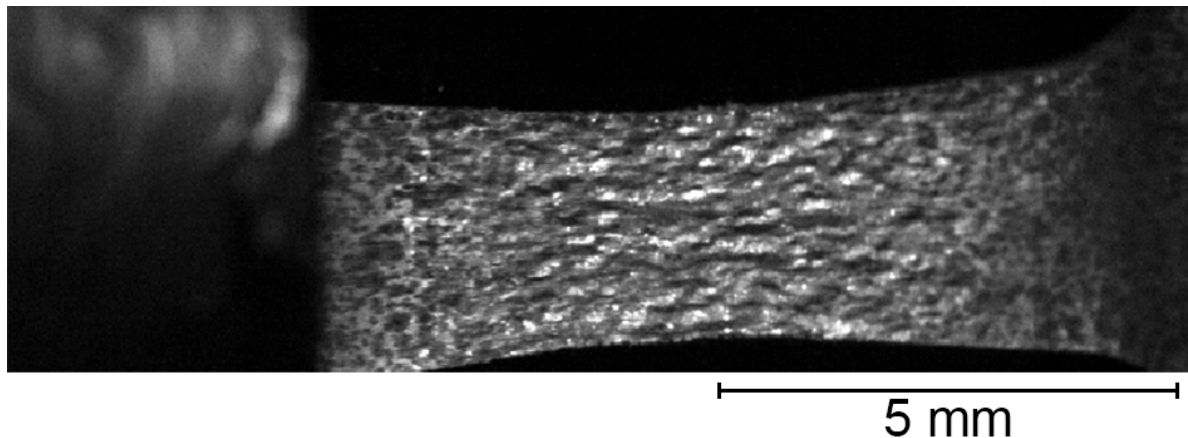


Figure 10. Optical image of the rough surface developed during deformation at 1120 °C.

Figure 11 shows an example of such a drop in radiometric temperature for a specimen with an average radiometric temperature of 700 °C. A second calibration curve had to be estimated to correct the radiometric temperature values to surface temperatures of the specimen where a rough surface developed at the beginning of plastic deformation. Interrupting the high strain rate deformation of the specimen at a given strain for a high-temperature test was not possible, and even if it would have been practically possible, the sample surface would very likely have had a considerable oxide layer on top of it after cooling down. A different approach had to be taken to obtain a calibration curve. As there is very little adiabatic heating in the specimen at very small strains, the average temperature of the specimen just before the yield point and slightly after the yield point should be almost the same. The average radiometric temperature measured from the center of the specimen just before the yield point was converted to surface temperature using the original calibration curve. The surface temperature of the specimen was assumed to be constant for a few percent of plastic deformation, and the radiometric temperature after yielding was assumed to correspond to the same surface temperature that was measured just prior to the yield point. A second-order polynomial function was used to model the calibration curves of the polished surface, while a linear fit was used for the rough surface.

Figure 12 shows the experimental calibration data with and without the IR filter, as well as the polynomial calibration curves for polished and rough surfaces for the commercially pure titanium with an integration time of 5 μ s, and surface temperatures from 20 up to 1400 °C. The standard error mean increases with temperature, but it is reasonably low until the surface temperatures of 1100 °C. The lower uncertainties (high accuracy) at lower temperatures are at least partly related to the more precise thermocouple measurements at low temperatures. The increase in the uncertainties at higher temperatures is also related to more prominent surface oxidation at the higher temperatures and to the difference in surface quality between specimens playing a bigger role when the material emitted the most radiation. An integrated calibration curve combining both calibration curves was tailored for each test, so that the calibration curve would smoothly change from one to the other according to how quickly the change in emissivity and consequent drop in radiometric temperatures occurred.

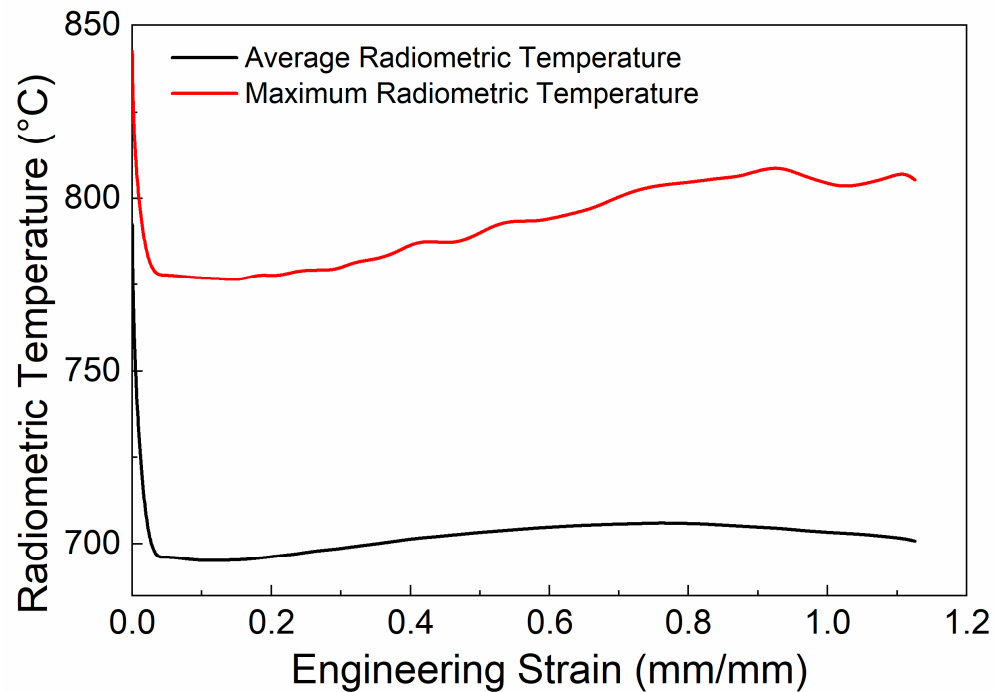


Figure 11. Sharp drop in average and maximum radiometric temperatures observed soon after the onset of plastic deformation.

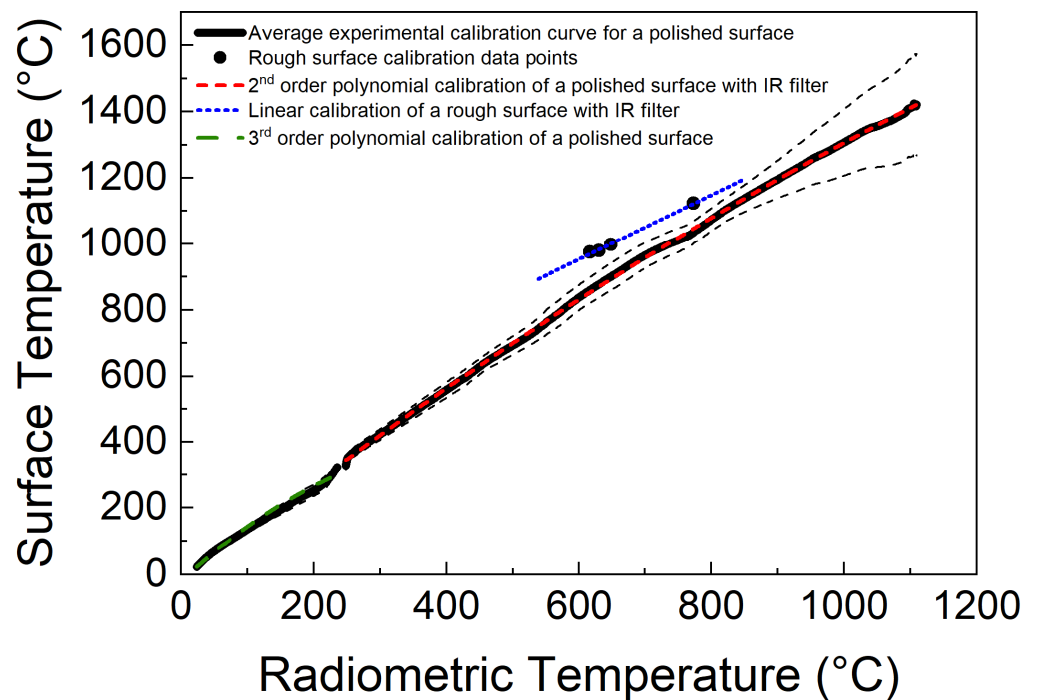


Figure 12. Experimental calibration data and polynomial temperature calibration curves for commercially pure titanium with polished and rough surfaces and with and without an attenuation IR filter. The average experimental calibration data is represented with their respective standard error of the means as dashed lines.

Figure 13 shows the surface temperature as a function of the engineering strain of a specimen which only required the smooth surface-temperature calibration, as well as an example where a drop in radiometric temperature due to the developed surface

roughness occurred and where the integrated calibration approach was used to mitigate this phenomenon. Although the integrated calibration did not completely eliminate the issue and did not work flawlessly for every specimen, the transition between the calibration curves is smooth and it makes the decrease in temperature considerably lower. The full-field temperature profile was also considered when analyzing the validity of such an approach, so that it would not address the issue in only a part of the specimen but would cover the entire specimen. It is important to note that the rougher surface only seemed to develop in the regions which had reached a certain critical temperature, so the outer sections of the sample still retained their polished surface, while the middle (hotter) section developed a rougher surface leading to difficulties in differentiating the areas. In this study, the emissivity was considered to be the same for the entire specimen and no gradient of emissivity was taken into account, which is satisfactory considering that the temperatures were calibrated for the central portion of the sample where most of the deformation occurred. This drop in the radiometric temperature during the lower strain values was not observed in specimens tested at higher radiometric temperatures (above 1050 °C). In the experiments where the sharp drop in radiometric temperature was not observed, only the smooth-surface calibration curve was used.

2.7. Uncertainties of the Temperature and Strain Measurements

The uncertainties of the displacements and strains measured by DIC were evaluated by averaging 10 stationary images of the unloaded sample at different temperatures and analyzing the standard deviation of these displacements, strains, stereo reconstruction errors, and radiometric temperatures. In such conditions, there should not be any detectable strains, and any measured strain would be associated with external uncertainty sources. The stereo reconstruction error (epipolar error) at different testing temperatures was also evaluated from the stationary images and are shown as an average and standard deviation as a function of radiometric temperature. Considering that the sample is virtually at the same temperature if imaged at a very high acquisition rate, the noise floor of the full-field temperature measurements was evaluated by averaging 10 thermal images of the heated sample shortly before the dynamic loading. These images were taken in approximately 160 μ s, and the heat diffusion during that time was very low. The radiometric temperature resolution was considered as the standard deviation of the radiometric temperature in the gage length of the specimens. Figure 14 shows the resolution of the displacement, strain, and temperature full-field measurements, as well as the average stereo reconstruction error as a function of the radiometric temperature. In all cases, the measured mean strain values were practically null. Furthermore, the displacement-, strain-, and temperature-noise floors were considerably lower than the quantities-of-interest observed during deformation. Although the stereo reconstruction error showed a much higher standard deviation at higher temperatures in comparison with that at room temperature, it was only twice as high at the highest investigated temperature. The decrease in the strain and displacement resolution, and the increase of the stereo reconstruction error with increasing temperature could be associated with many factors, such as distortions caused by heated air in the vicinity of the hot specimen, degradation of the pattern due to the high temperature, and interference of the incandescent radiation in the gray levels recorded by the optical cameras. However, considering that only a small section of the specimen is at the testing temperature, the uncertainties caused by the air distortions should be lower than for testing systems where more elements of the setup are at high temperatures. The increase in the resolution of the radiometric temperature is probably related to the better signal-to-noise ratio at higher temperatures. In addition, according to the infrared camera manufacturer, the maximum expected uncertainty for the temperature measurements is of ± 1 °C or $\pm 1\%$ from 0 to 200 °C, and 2 °C or $\pm 2\%$ from 200 to 1500 °C. Therefore, the highest expected deviation, at the highest radiometric temperature investigated in this work, would be of approximately 20 °C. The overall resolution and accuracy of the method seem quite reasonable for most high-strain rate materials science and engineering research.

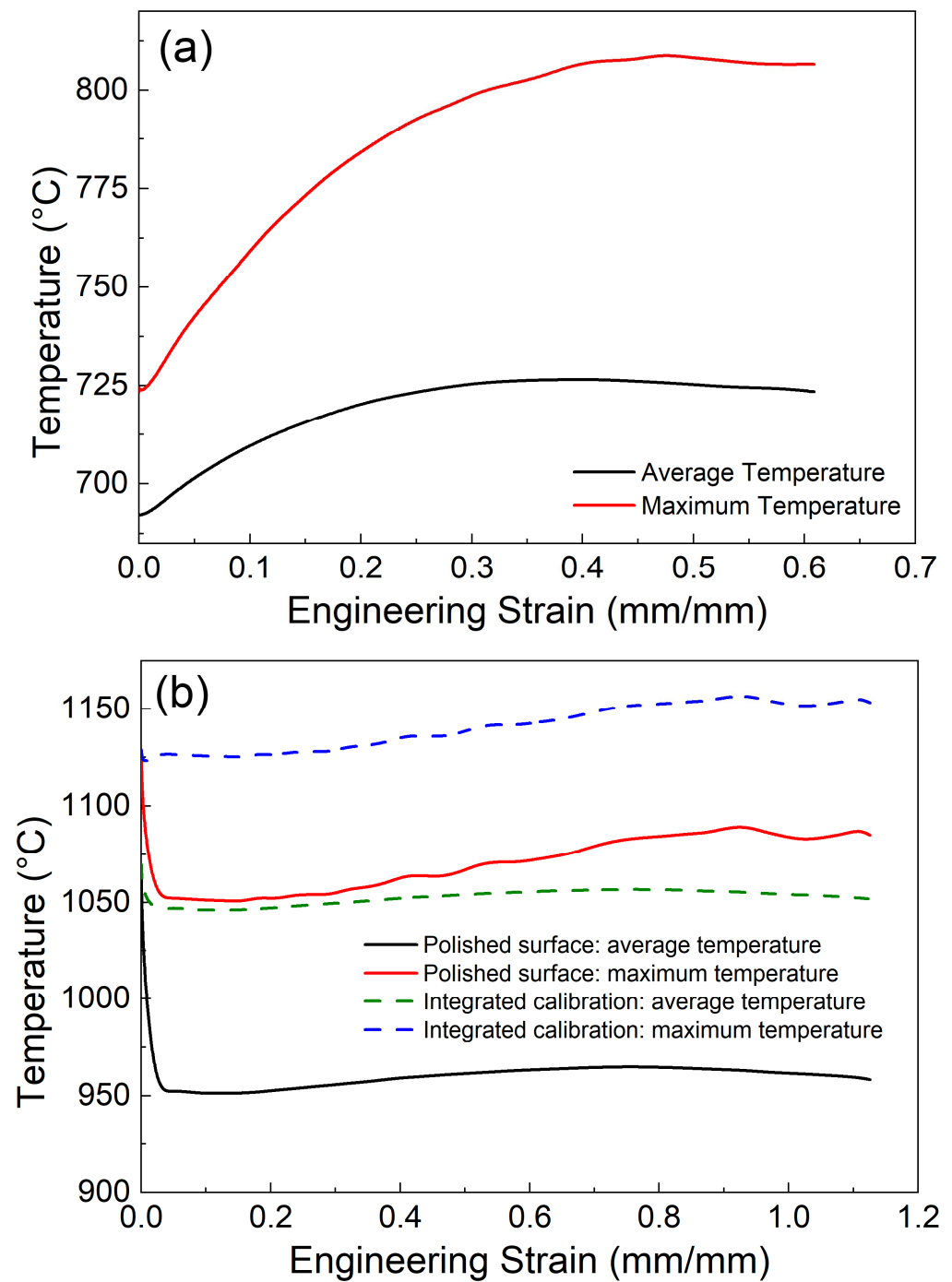


Figure 13. Average and maximum temperatures as a function of engineering strain for (a) a specimen with constant emissivity and (b) a specimen where rapid change in emissivity causes a significant drop in radiometric temperature in the beginning of deformation. The solid lines represent the temperature values calibrated by the smooth surface-temperature calibration and the dashed lines represent the values obtained from the integrated calibration.

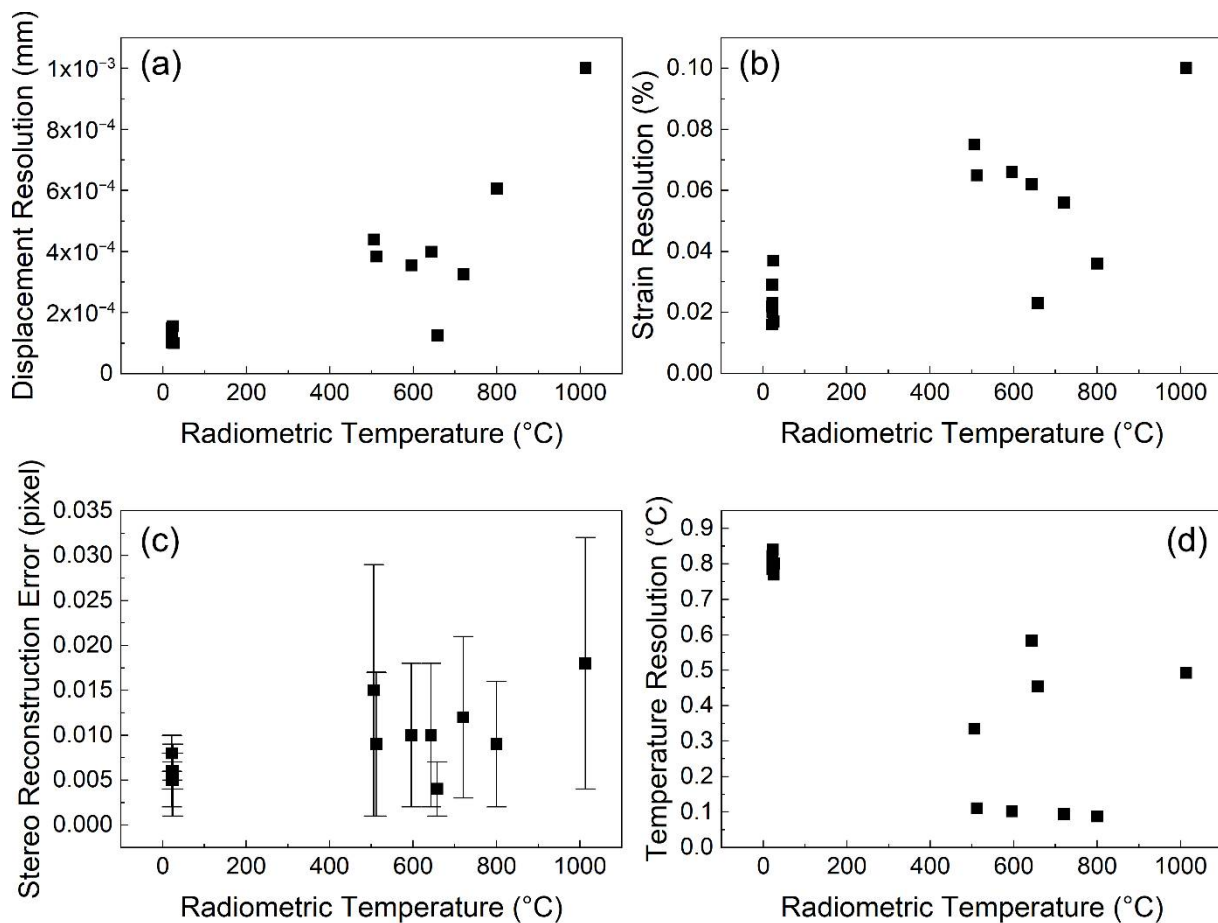


Figure 14. Uncertainties of the full-field quantities-of-interest of the DIC and IRT measurements as a function of radiometric temperature. (a) Displacement, (b) strain, (c) stereo reconstruction error, and (d) radiometric temperature. The error bars represent the standard deviation of the stereo reconstruction error throughout the sample gage length.

3. Results and Discussion

The engineering stress–strain curves obtained from the tensile tests at room temperature up to 1120 °C at a strain rate of approximately 1000 up to 1600 s^{-1} are shown in Figure 15. The test at room temperature had a strain rate of 1000 s^{-1} and the tests at elevated temperatures had a strain rate of approximately 1600 s^{-1} . The yield strength of the commercially pure titanium decreased from 575 MPa at room temperature to 67 MPa at 700 °C, and to 30 MPa at 1120 °C. The mechanical strength of the commercially pure titanium observed in the current work is in accordance with that reported at similar temperature ranges (up to 700 °C) for commercially pure titanium in dynamic [48] and quasi-static tests [49,50]. It is noteworthy that the onset of necking occurred at a lower plastic strains in the current work than those reported in the literature [48–50]. The ductility of the material increased from 40% at room temperature to almost 100% at 950 °C. Up to 15% of uniform deformation was observed at room temperature before necking, but the onset of necking occurred almost instantly after yielding at temperatures from 700 to 1120 °C. The specimens at high temperatures (≥ 1120 °C) did not break during the first loading pulse, so the maximum engineering strain in the stress–strain curves does not correspond to the failure strain. The noisier stress signals at elevated temperatures are due to the much lower mechanical resistance of the material, leading to a lower strain signal measured by the strain gage on the transmitted bar. Some level of noise is inevitable in these experiments, despite an aluminum bar with a much lower elastic modulus having been used to improve the resolution of the measurements and the loading pulses FFT-filtered, as described earlier.

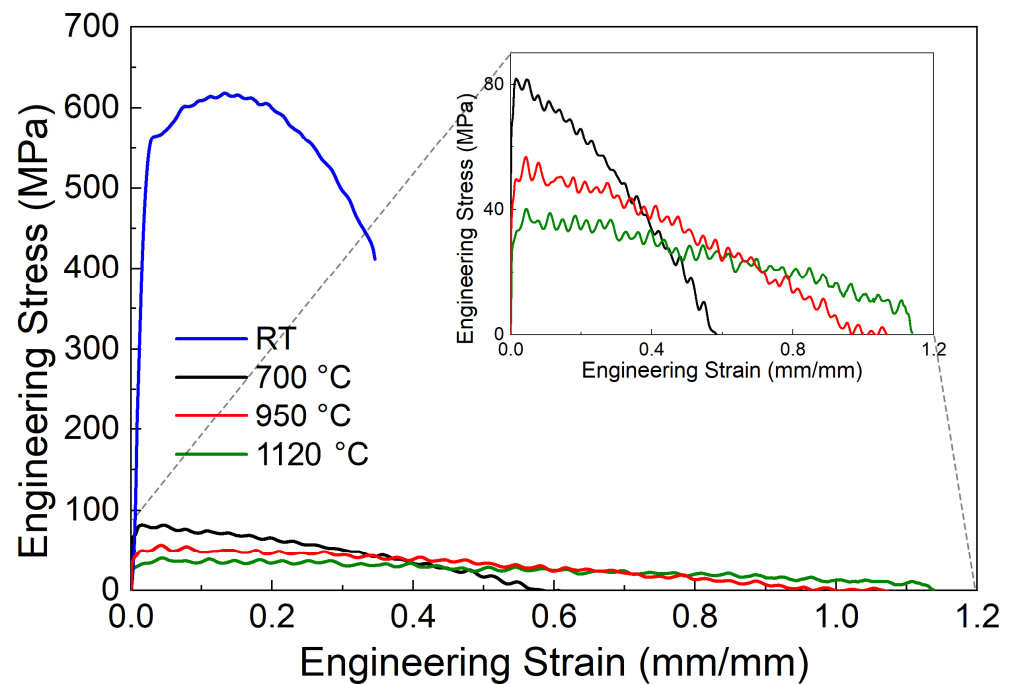


Figure 15. Engineering stress–strain plots for commercially pure titanium in tension at temperatures from room temperature up to 1120 °C and at strain rates from 1000 up to 1600 s^{−1}. The zoomed-in section shows the stress–strain plots at elevated temperatures in more detail.

At room temperature, commercially pure titanium is composed of α -Ti phase with a hexagonal close-packed crystal structure, and it has an allotropic phase transformation at 860–960 °C [51] to a β -Ti phase with a body-centered cubic crystallographic structure. Therefore, the mechanical response of the material at high temperatures (950 and 1120 °C) is influenced by both the temperature and the different mechanical properties and behaviors of the β -Ti, as is evidenced by the much higher ductility at 950–1120 °C. This phase transformation occurs almost instantly. According to the literature, the time that it takes for the phase transformation to complete varies between less than 200 μ s [52] and approximately 60 ms [53]. The transformation temperature increases with heating rate and the temperature during the transformation is not necessarily constant for very high heating rates [54]. In the current work, the specimen was at the target temperature for at least 0.3 s prior to the mechanical testing, and so the phase transformation was completed before the loading of the specimen in the tests carried out above the transformation temperature. According to Kaschnitz and Reiter [54], the transformation temperature increased by 20 °C when the heating rate was 3800 K/s. In the current work, the heating rates are slower than that, and therefore, the transformation temperature would have been increased by less than 20 °C, and the heating rate would have not affected the test carried out at 950 °C. The phase transformation is fast, and as the loading occurs rapidly after the heating, there is not much time for grain growth and other reorganizations of the microstructure. Therefore, this experiment better simulates cases where the temperature of the material increases fast and is soon followed by the dynamic loading, for example chip formation in high-speed machining, whereas other experiments may be better suited for experimental investigations of, for example, high-temperature forging, where the material is kept at high temperatures for longer periods of time before the dynamic loading.

The evolution of the full-field axial strains and surface temperatures of specimens deformed at room temperature, 700 °C, and 1120 °C are, respectively, shown in Figures 16–18. In these Figures, the evolution of strain and temperature are represented as maps that are overlaid over the optical images and represented on the same coordinate system and frame of reference. Considering that the behavior of the specimen tested at 950 °C was

something between that observed at 700 and 1120 °C, the full-field measurements of this test are not presented here for the sake of brevity. At room temperature, the deformation and temperature rise were uniform up to approximately 0.15 engineering strain where necking started. The onset of necking is evident by the rapid localization of strain and heat release in the central regions of the specimen, which ultimately leads to axial strains of up to 1.08 associated with an increase in temperature of several hundreds of degrees. The infrared camera sensor consistently saturates during the rupture of the sample, so the maximum temperatures measured in the full-field maps in Figure 16 are not actually the highest temperatures that the specimen reaches during high-strain deformation at room temperature. Surface temperatures as high as 463 °C have been measured during fracture, when the infrared camera was equipped with an attenuation filter.

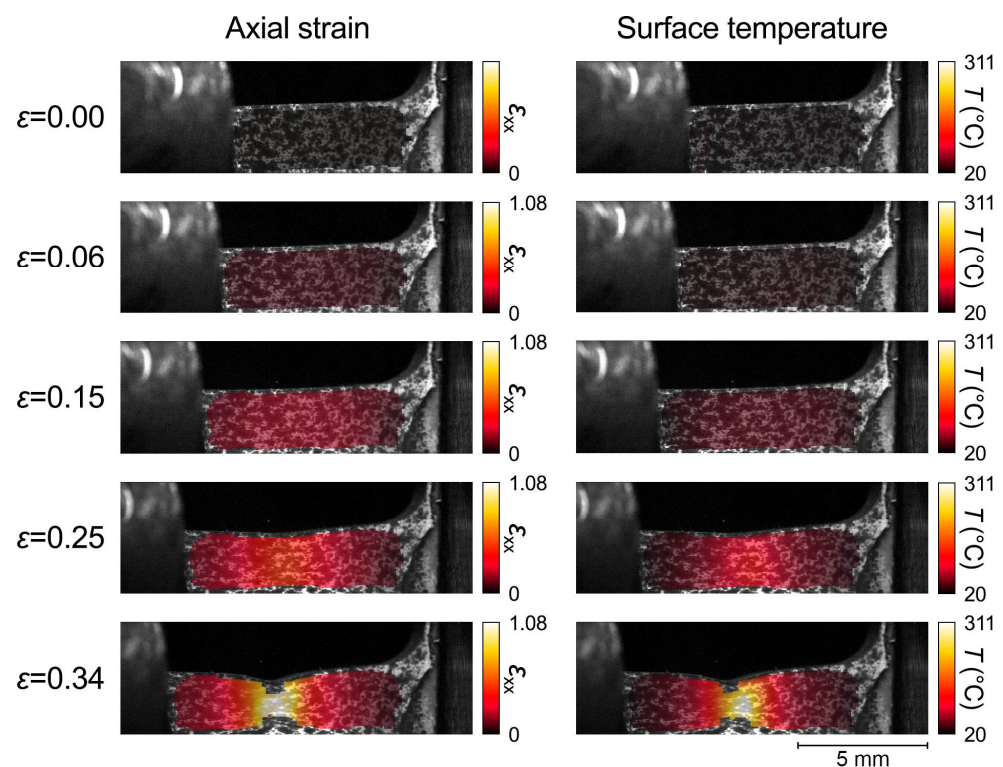


Figure 16. Full-field axial strain and surface temperature at different global engineering strains in a commercially pure titanium specimen loading in tension at room temperature and a strain rate of approximately 1000 s^{-1} .

In the test at 700 °C, the temperature in most parts of the specimen's gage length is uniform (Figure 17), although a temperature gradient is observed as the outer regions of the gage section are at a lower temperature than that of the central part of the specimen. This occurs as the electrical resistive heating system only heats up the gage length of the sample, and there is enough time for some heat transfer to occur after the heating of the specimen. The onset of necking occurs almost instantly after yielding at 700 °C, and the material shows a much more non-uniform deformation than at room temperature, reaching axial strains up to approximately 4.5. A temperature increase up to 80 °C was observed during plastic deformation and necking at 700 °C. Deformation occurred mostly in the heated-up portion of the specimen, and adiabatic heating was as localized as at room temperature.

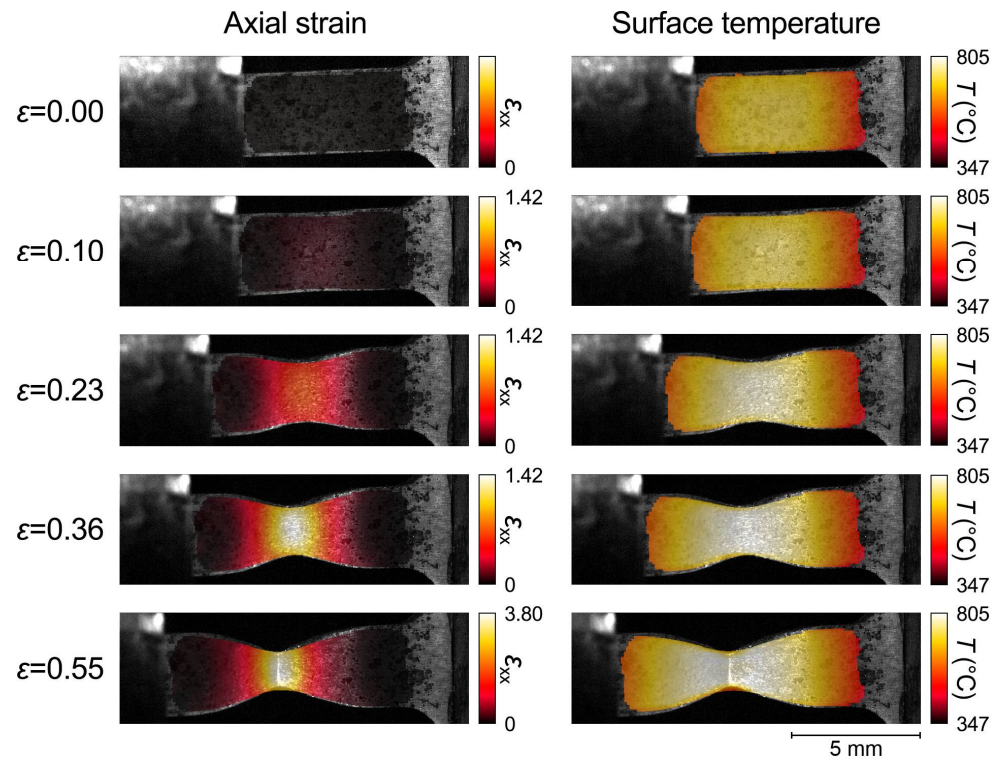


Figure 17. Full-field axial strains and surface temperatures at different global engineering strains in a commercially pure titanium specimen loaded in tension at an average initial temperature of 700 °C and a strain rate of approximately 1600 s⁻¹.

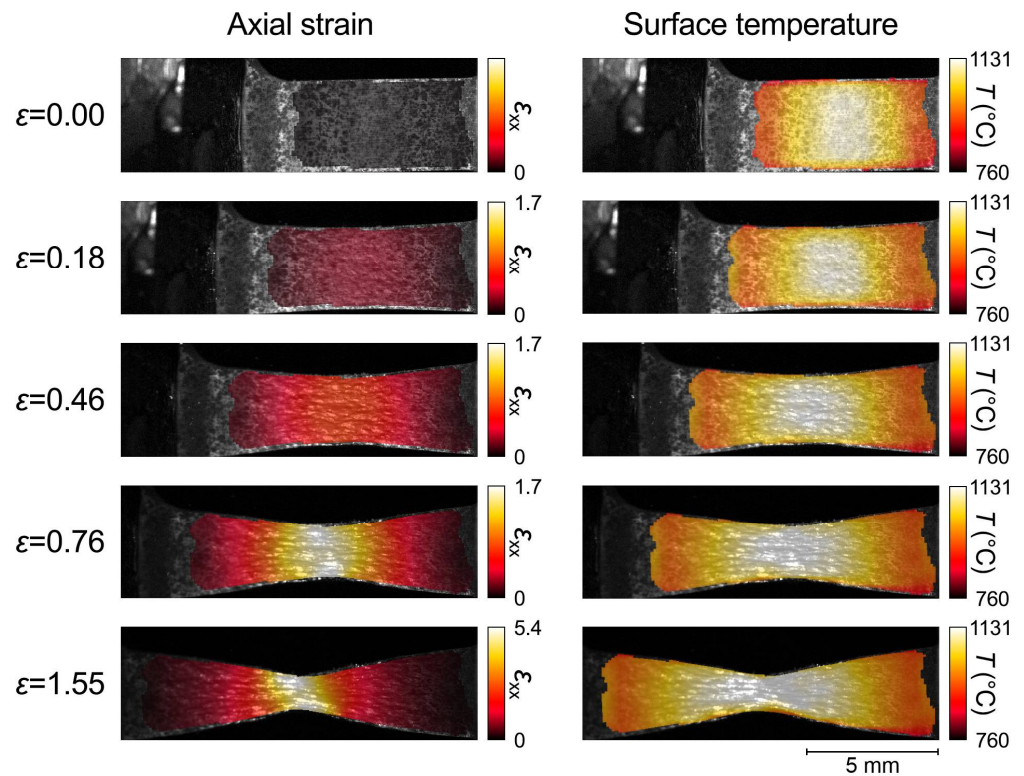


Figure 18. Full-field axial strains and surface temperatures at different global engineering strains in a commercially pure titanium specimen loaded in tension at an average initial temperature of 1120 °C and a strain rate of approximately 1600 s⁻¹.

At 1120 °C, necking initially occurred throughout most of the gauge section of the specimen, which can be observed at an engineering strain of 0.46 in Figure 18. Although the deformation became more localized at higher strains ($\epsilon = 0.76$ and 1.55), considerable deformation still occurred on the outermost sections of the specimen, where temperatures were lower than that in the center. The reason for necking not concentrating on the white region of the full-field temperature map is that even though there is a temperature gradient in the specimen, the orange regions of the temperature map are still as high as 1050 °C, and do not have much more mechanical resistance than the central portion of the specimen. Despite having reached axial strains as high as 5.4, the specimen was much more ductile and did not break during the first loading pulse, only breaking on the second loading pulse at 1120 °C. Contrarily to what was observed at 700 °C, there was no observable adiabatic heating in the test at 1120 °C, and the temperature gradient in the specimen remained roughly constant throughout deformation. The seemingly seamless transition between the first and the second full-field temperature maps of the specimen tested at 1120 °C (Figure 18) is further evidence that the integrated calibration procedure worked reasonably well to address the decrease in emissivity observed during this test.

Figure 19 shows 3D waterfall plots of the full-field deformation and temperature along the gage length of the specimen as a function of global engineering strain for specimens deformed at room temperature, 700 °C, and 1120 °C. These waterfall plots depict the full-field data from a horizontal line along the centerline of the specimen and show the strain and temperature evolution up to either fracture or the end of the first loading pulse. They are plotted in the same Lagrangian frame of reference, which makes it easier to compare different tests to one another and to follow the evolution of strain or temperature localizations in a given material coordinate during deformation. The shape of the waterfall plots at room temperature is different from those at higher temperature, as at room temperature the strain localizes less before fracture and there is a higher temperature increase during necking. In the test performed at an initial temperature of 700 °C, the temperature during necking stopped increasing at an engineering strain of approximately 0.5, even though there was still significant strain localization until fracture at a global engineering strain of 0.6. The adiabatic heating clearly stopped, and furthermore, there was a decrease in temperature in the very middle of the necking region where the strain was most localized. This decrease of temperature during necking was observed in multiple specimens, it was also observed in the raw radiometric temperature data and is not a result of the calibration procedure. In this particular specimen, this occurred in the very center of the specimen where the strain localized the most over the course of seven images. The drop in temperature was observed in multiple different sensor pixels, so it is not a temporal or spatial resolution issue. Furthermore, the radiometric temperature continued decreasing as the strain localized further, as though this could have been a result of a local drop in emissivity caused by the massive strain localization during necking. No considerable increase or decrease in the temperature during necking was observed in the specimen tested at 1120 °C, even though it had even higher strain localization than that tested at 700 °C. The temperature of the specimen tested at 1120 °C decreased slightly at the beginning of the deformation, even with the integrated calibration, and this can be visualized in the temperature waterfall plot. The difference between the necking at 1120 °C and the more localized necking at 700 °C is more evident in the waterfall plots, and it is easier to compare them to one another. While the region with 100% axial strains at 1120 °C spans for approximately 2 mm, it is only 1-mm wide in the specimen tested at 700 °C. Although necking started earlier, it can be seen from the waterfall plots that there is a critical strain at which the strain localization occurs at a faster rate and ultimately leads to fracture. This critical strain value was a function of temperature, of approximately 0.25, 0.3 and 0.8 for the tests at room temperature, 700 and 1120 °C, respectively.

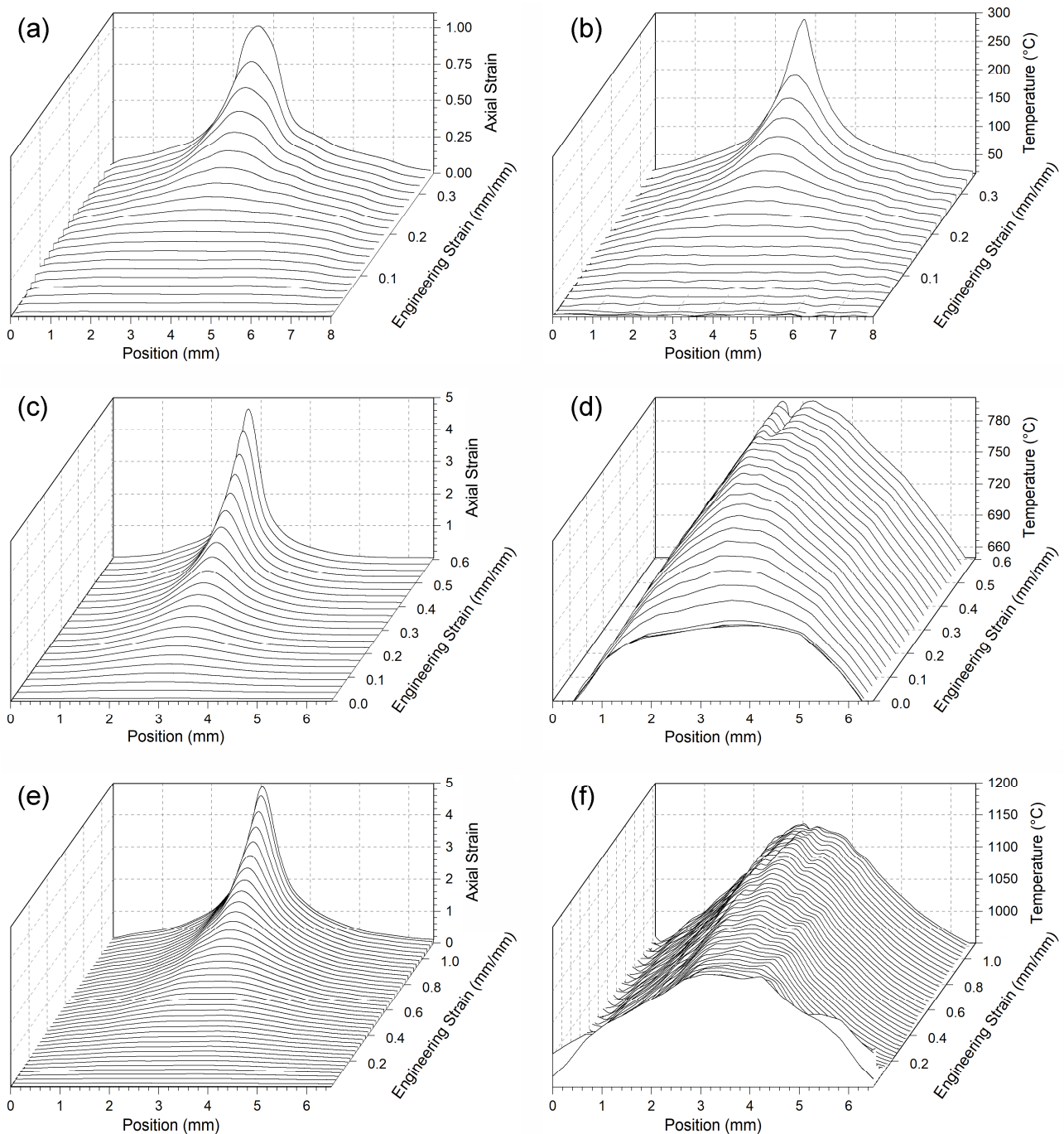


Figure 19. Three-dimensional waterfall plots of axial strain (a,c,e) and surface temperature (b,d,f) of commercially pure titanium tested in tension at a strain rate of approximately 1600 s^{-1} at (a,b) room temperature, (c,d) $700 \text{ }^\circ\text{C}$, and (e,f) $1120 \text{ }^\circ\text{C}$.

The temperature gradients in the specimens tested at 700 and $1120 \text{ }^\circ\text{C}$ are evident when analyzing the temperature distribution with waterfall plots in Figure 19. The gradients are a drawback of the electrical resistive heating system, as only the gauge length of the specimen is heated up. The specimen starts cooling fast when the heating stops, and if enough time elapses prior to the mechanical loading of the specimen, some of the heat is transferred to the grip sections of the dog-bone specimen and, eventually, even to the bars. The specimen tested at $700 \text{ }^\circ\text{C}$ had a region of 4 mm with almost uniform temperature, but at $1120 \text{ }^\circ\text{C}$, the region where the temperature was uniform was approximately 2 mm long.

It is logical that the magnitude of the temperature gradient inside the specimen increases with testing temperature, as the temperature difference between the hot specimen and the environment increases. There is a 50 °C gradient in the specimen tested at 700 °C (Figure 19) and a 120 °C gradient in the specimen tested at 1120 °C. As the flow stress of the material decreases with temperature, deformation occurs mostly in the region where the temperature is the highest. The regions at lower temperatures also deform elastically and plastically if the load reaches the flow stress of those regions during the test. The influence of the temperature gradient on the deformation of the specimen depends on how the mechanical resistance of the material varies in the given temperature range of the gradient. At 1120 °C, the strength of the material is more or less the same in the temperature range of the gradient, and practically the entire gage section of the specimen deforms plastically. At 700 °C, the strength of the material changes more within the range of the temperature gradient, which ultimately leads to a more focused localization of the deformation in the hottest portion of the specimen. Nevertheless, the load or engineering stress measurements are not affected by the temperature gradient, and represent the load carried by the specimen. Considering that the original cross-sectional area of the specimen is used to calculate the engineering stress, its calculation is also valid even with such a temperature gradient. With an increasing stress mainly deforming the hottest portion of a specimen, the outer sections would also still be deformed to a lesser extent. Having a temperature and strain gradient in a specimen would be an issue for the conventional strain measurements using the strain-gage measurements, which rely solely on an initial gauge length, but it is a challenge that can be dealt with if the temperature and strain gradients in the specimen are known. It is clear that the full-field strain and temperature measurements facilitate material characterization at extreme conditions, even when small temperature gradients are present.

4. Conclusions

This work describes a method for full-field strain and temperature measurements for materials tested at high temperatures and high strain rates by integrating synchronized DIC and IRT, an electrical resistive heating system, and a tensile SHPB. The full-field thermomechanical behavior of commercially pure titanium was investigated at strain rates up to approximately 1600 s⁻¹ and temperatures up to 1120 °C. The paper highlights the following novelties:

- The full-field strain and temperature measurements of high strain-rate tension tests for titanium at elevated temperatures were successfully temporally and spatially synchronized. The strain and temperature evolutions during the uniform deformation and necking of titanium at elevated temperatures were monitored with high temporal and spatial resolution;
- A decrease in mechanical strength and increase in ductility were observed with increasing temperature. The local strains in the neck also increased considerably with temperature. The critical strain at which the rate of strain localization increased rapidly was higher at higher testing temperatures;
- A temperature increase as high as 80 °C was observed at 700 °C, despite the low strength of the material and the consequent low applied mechanical work. A decrease in the radiometric temperature was observed during necking at 700 °C, which can at least partly be explained by a local decrease in emissivity due to the massive strain localization after reaching approximately 200% axial strain. No considerable adiabatic heating was observed at higher testing temperatures;
- The resistive electric heating generated a temperature gradient along the gage section of the specimen, but as the strength of the material at 1120 °C does not strongly depend on temperature, the specimen deformed throughout the gage length of the specimen. At 700 °C, the material response depended on the temperature more strongly, and the necking was more localized even though the gradient was smaller;

- A blue-green shortpass filter and high-temperature-resistant engine manifold spray paints were used to enable DIC at high temperatures where the material is incandescent. An infrared attenuation filter was used enable IRT data acquisition at a wide range of temperatures. The contrast of a painted pattern imaged with the shortpass filter was reduced by 50% at a temperature of 880 °C, but still retained sufficient contrast for DIC;
- Calibration curves were constructed to convert radiometric temperature values to true surface temperature values by monitoring the temperature of a cooling sample with the infrared camera and thermocouples. An extra temperature calibration curve and an integrated calibration approach were used to address the substantial drop in radiometric temperature caused by the formation of a rougher surface texture during deformation in a given range of temperatures;
- The uncertainties of DIC and IRT were evaluated as a function of testing temperature, and while there was a decrease in the displacement and strain resolution with temperature, they were still adequate for the measurements at elevated temperatures;
- The full-field strain and temperature data were presented as both full-field maps and 3D waterfall plots of strain and temperature as a function of position along the gage length and global engineering strain.

This method looks very promising for studying material behavior in applications where high strain rates occur at high temperatures, as the acquired data can be used for constitutive modelling, finite element analysis, and inverse modeling approaches. Such large amounts of data can be also useful for machine-learning purposes and other statistical or data-driven modeling approaches. Furthermore, this method produces additional data that facilitates the description of the material behavior, especially for such materials where the onset of necking occurs very quickly after yielding. The full-field approach complements the standard Hopkinson Bar analytics with local strain and temperature information. The full-field techniques are going to play an important role in furthering our understanding of necking, strain localization, failure mechanisms, and their relationship with material properties under extreme conditions.

Author Contributions: Conceptualization, M.H.; Data curation, G.C.S.; Formal analysis, Funding acquisition, M.H.; Investigation, G.C.S.; Methodology, G.C.S.; Project administration, M.H.; Resources, M.H.; Software, G.C.S.; Supervision, M.H.; Visualization, G.C.S.; Writing—original draft, G.C.S.; Writing—review and editing, G.C.S. and M.H. All authors have read and agreed to the published version of the manuscript.

Funding: This research was funded by the Air Force Office of Scientific Research (AFOSR).

Data Availability Statement: The raw/processed data required to reproduce these findings cannot be shared at this time due to technical or time limitations. The data can be made available upon reasonable request to the corresponding author.

Conflicts of Interest: The authors declare no conflict of interest. The funders had no role in the design of the study; in the collection, analyses, or interpretation of data; in the writing of the manuscript, or in the decision to publish the results.

References

1. Sastry, S.M.L.; Pao, P.S.; Sankaran, K.K. *High Temperature Deformation of Ti-6Al-4V*; Kimura, H., Izumi, O., Eds.; Metallurgical Society of AIME: Warrendelae, PA, USA, 1980.
2. Lee, W.-S.; Lin, C.-F. High-temperature deformation behaviour of Ti6Al4V alloy evaluated by high strain-rate compression tests. *J. Mater. Process. Technol.* **1998**, *75*, 127–136. [[CrossRef](#)]
3. Gangireddy, S.; Mates, S.P. High-Strain-Rate Deformation of Ti-6Al-4V Through Compression Kolsky Bar at High Temperatures. In *Dynamic Behavior of Materials*; Springer: Cham, Switzerland, 2017; Volume 1, pp. 215–220. ISBN 9783319411316.
4. Bruschi, S.; Poggio, S.; Quadrini, F.; Tata, M.E. Workability of Ti-6Al-4V alloy at high temperatures and strain rates. *Mater. Lett.* **2004**, *58*, 3622–3629. [[CrossRef](#)]
5. Liu, Q.; Hui, S.; Tong, K.; Yu, Y.; Ye, W.; Song, S.-y. Investigation of high temperature behavior and processing map of Ti-6Al-4V-0.11Ru titanium alloy. *J. Alloys Compd.* **2019**, *787*, 527–536. [[CrossRef](#)]

6. Hueto, F.; Hokka, M.; Sancho, R.; Rämö, J.; Östman, K.; Gálvez, F.; Kuokkala, V.-T. High Temperature Dynamic Tension Behavior of Titanium Tested with Two Different Methods. *Procedia Eng.* **2017**, *197*, 130–139. [[CrossRef](#)]
7. Lee, W.-S.; Lin, C.-F.; Huang, S.-Z. Effect of temperature and strain rate on the shear properties of Ti-6Al-4V alloy. *Proc. Inst. Mech. Eng. Part C J. Mech. Eng. Sci.* **2006**, *220*, 127–136. [[CrossRef](#)]
8. Walley, S.M. The Effect of Temperature Gradients on Elastic Wave Propagation in Split Hopkinson Pressure Bars. *J. Dyn. Behav. Mater.* **2020**, *6*, 278–286. [[CrossRef](#)]
9. Leotoing, L.; Guines, D.; Robin, E.; Le Cam, J.B. Effects of Strain Path Changes on the Kinematics and the Intrinsic Dissipation Accompanying PLC Bands in Al-Mg Alloys. *Exp. Mech.* **2019**, *59*, 963–977. [[CrossRef](#)]
10. Pan, B.; Wu, D.; Wang, Z.; Xia, Y. High-temperature digital image correlation method for full-field deformation measurement at 1200 °C. *Meas. Sci. Technol.* **2011**, *22*, 015701. [[CrossRef](#)]
11. Novak, M.D.; Zok, F.W. High-temperature materials testing with full-field strain measurement: Experimental design and practice. *Rev. Sci. Instrum.* **2011**, *82*, 115101. [[CrossRef](#)]
12. Wang, W.; Xu, C.; Jin, H.; Meng, S.; Zhang, Y.; Xie, W. Measurement of high temperature full-field strain up to 2000 °C using digital image correlation. *Meas. Sci. Technol.* **2017**, *28*, 035007. [[CrossRef](#)]
13. Guo, X.; Liang, J.; Tang, Z.; Cao, B.; Yu, M. High-temperature digital image correlation method for full-field deformation measurement captured with filters at 2600 °C using spraying to form speckle patterns. *Opt. Eng.* **2014**, *53*, 063101. [[CrossRef](#)]
14. Valeri, G.; Koohbor, B.; Kidane, A.; Sutton, M.A. Determining the tensile response of materials at high temperature using DIC and the Virtual Fields Method. *Opt. Lasers Eng.* **2017**, *91*, 53–61. [[CrossRef](#)]
15. Pan, Z.; Huang, S.; Su, Y.; Qiao, M.; Zhang, Q. Strain field measurements over 3000 °C using 3D-Digital image correlation. *Opt. Lasers Eng.* **2020**, *127*, 105942. [[CrossRef](#)]
16. Marchand, A.; Duffy, J. An experimental study of the formation process of adiabatic shear bands in a structural steel. *J. Mech. Phys. Solids* **1988**, *36*, 251–283. [[CrossRef](#)]
17. Zhou, M.; Ravichandran, G.; Rosakis, A.J. Dynamically propagating shear bands in impact-loaded prenotched plates—II. Numerical simulations. *J. Mech. Phys. Solids* **1996**, *44*, 1007–1021. [[CrossRef](#)]
18. Zehnder, A.T.; Rosakis, A.J. On the temperature distribution at the vicinity of dynamically propagating cracks in 4340 steel. *J. Mech. Phys. Solids* **1991**, *39*, 385–415. [[CrossRef](#)]
19. Orteu, J.J.; Rotrou, Y.; Sentenac, T.; Robert, L. An innovative method for 3-D shape, strain and temperature full-field measurement using a single type of camera: Principle and preliminary results. *Exp. Mech.* **2008**, *48*, 163–179. [[CrossRef](#)]
20. Tang, Y.; Yue, M.; Fang, X.; Feng, X. Synchronous full-field measurement of temperature and deformation based on separated radiation and reflected light. *Opt. Lasers Eng.* **2019**, *116*, 94–102. [[CrossRef](#)]
21. Cholewa, N.; Summers, P.T.; Feih, S.; Mouritz, A.P.; Lattimer, B.Y.; Case, S.W. A Technique for Coupled Thermomechanical Response Measurement Using Infrared Thermography and Digital Image Correlation (TDIC). *Exp. Mech.* **2016**, *56*, 145–164. [[CrossRef](#)]
22. Chrysochoos, A.; Huon, V.; Jourdan, F.; Muracciotte, J.-M.; Peyroux, R.; Wattrisse, B. Use of full-field digital image correlation and infrared thermography measurements for the thermomechanical analysis of material behaviour. *Strain* **2010**, *46*, 117–130. [[CrossRef](#)]
23. Smith, J.L.; Seidt, J.D.; Gilat, A. Full-Field Determination of the Taylor-Quinney Coefficient in Tension Tests of Ti-6Al-4V at Strain Rates up to 7000 s⁻¹. In *Advancement of Optical Methods & Digital Image Correlation in Experimental Mechanics*; Springer: Cham, Switzerland, 2019; Volume 3, pp. 133–139. ISBN 9783319974811.
24. Seidt, J.D.; Kuokkala, V.-T.; Smith, J.L.; Gilat, A. Synchronous Full-Field Strain and Temperature Measurement in Tensile Tests at Low, Intermediate and High Strain Rates. *Exp. Mech.* **2017**, *57*, 219–229. [[CrossRef](#)]
25. Gilat, A.; Kuokkala, V.-T.; Seidt, J.D.; Smith, J.L. Full-Field Measurement of Strain and Temperature in Quasi-Static and Dynamic Tensile Tests on Stainless Steel 316L. *Procedia Eng.* **2017**, *207*, 1994–1999. [[CrossRef](#)]
26. Vazquez-Fernandez, N.I.; Soares, G.C.; Smith, J.L.; Seidt, J.D.; Isakov, M.; Gilat, A.; Kuokkala, V.T.; Hokka, M. Adiabatic Heating of Austenitic Stainless Steels at Different Strain Rates. *J. Dyn. Behav. Mater.* **2019**, *5*, 221–229. [[CrossRef](#)]
27. Soares, G.C.; Patnamsetty, M.; Peura, P.; Hokka, M. Effects of Adiabatic Heating and Strain Rate on the Dynamic Response of a CoCrFeMnNi High-Entropy Alloy. *J. Dyn. Behav. Mater.* **2019**, *5*, 320–330. [[CrossRef](#)]
28. Nie, Y.; Claus, B.; Gao, J.; Zhai, X.; Kedir, N.; Chu, J.; Sun, T.; Fezzaa, K.; Chen, W.W. In Situ Observation of Adiabatic Shear Band Formation in Aluminum Alloys. *Exp. Mech.* **2020**, *60*, 153–163. [[CrossRef](#)]
29. Tarfaoui, M.; El Moumen, A.; Ben Yahia, H. Damage detection versus heat dissipation in E-glass/Epoxy laminated composites under dynamic compression at high strain rate. *Compos. Struct.* **2018**, *186*, 50–61. [[CrossRef](#)]
30. Shen, L.; Hui, M.; Liu, Y. Strain Rate Dependence of Hardness for PE and SME TiNi Alloys. *Metals* **2020**, *10*, 1157. [[CrossRef](#)]
31. Liu, Y.; Shan, L.; Shan, J.; Hui, M. Experimental study on temperature evolution and strain rate effect on phase transformation of TiNi shape memory alloy under shock loading. *Int. J. Mech. Sci.* **2019**, *156*, 342–354. [[CrossRef](#)]
32. Tang, Y.; Zhang, J.; Yue, M.; Zhu, X.; Fang, X.; Feng, X. High-frequency flashing of light source for synchronous measurement of temperature and deformation at elevated temperature. *Opt. Lasers Eng.* **2021**, *137*, 106361. [[CrossRef](#)]
33. Crump, D.A.; Dulieu-Barton, J.M.; Fruehmann, R.K. Challenges in synchronising high speed full-field temperature and strain measurement. In *Thermomechanics and Infra-Red Imaging*; Conference Proceedings of the Society for Experimental Mechanics Series; Springer: New York, NY, USA, 2011; Volume 7, pp. 1–7.

34. Gorham, D.A.; Wu, X.J. An Empirical Method of Dispersion Correction in the Compressive Hopkinson Bar Test. *Le J. Phys. IV* **1997**, *7*, 223–228. [[CrossRef](#)]
35. Hokka, M. *Effects of Strain Rate and Temperature on the Mechanical Behavior of Advanced High Strength Steels*; Tampere University of Technology: Tampere, Finland, 2008.
36. Isakov, M.; Östman, K.; Kuokkala, V.T. Metastable austenitic steels and strain rate history dependence. In *Challenges In Mechanics of Time-Dependent Materials and Processes in Conventional and Multifunctional Materials*; Conference Proceedings of the Society for Experimental Mechanics Series; Springer: Cham, Switzerland, 2014; Volume 2, pp. 99–108.
37. Curtze, S. *Characterization of the Dynamic Behavior and Microstructure Evolution of High Strength Sheet Steels*; Tampere University of Technology: Tampere, Finland, 2009.
38. Soares, G.C.C.; Vázquez-Fernández, N.I.I.; Hokka, M. Thermomechanical Behavior of Steels in Tension Studied with Synchronized Full-Field Deformation and Temperature Measurements. *Exp. Tech.* **2021**, *45*, 627–643. [[CrossRef](#)]
39. LaVision, 3D Calibration Plate for StrainMaster: Validated calibration plates, 21 December 2021. Available online: <https://www.lavision.de/en/download.php?id=3678> (accessed on 1 November 2021).
40. Bigger, R.; Blaysat, B.; Boo, C.; Grewer, M.; Hu, J.; Jones, A.; Klein, M.; Raghavan, K.; Reu, P.; Schmidt, T.; et al. *A Good Practices Guide for Digital Image Correlation*; Jones, E., Iadicola, M., Eds.; 2018; Available online: https://idics.org/guide/DICGoodPracticesGuide_PrintVersion-V5h-181024.pdf (accessed on 1 November 2021). [[CrossRef](#)]
41. Rittel, D. Transient temperature measurement using embedded thermocouples. *Exp. Mech.* **1998**, *38*, 73–78. [[CrossRef](#)]
42. Rittel, D. Experimental investigation of transient thermoelastic effects in dynamic fracture. *Int. J. Solids Struct.* **1998**, *35*, 2959–2973. [[CrossRef](#)]
43. Rittel, D. On the conversion of plastic work to heat during high strain rate deformation of glassy polymers. *Mech. Mater.* **1999**, *31*, 131–139. [[CrossRef](#)]
44. Walley, S.M.; Proud, W.G.; Rae, P.J.; Field, J.E. The dynamic temperature measurement of split Hopkinson bar specimens using small thermocouples and infrared streak photography. In *Proceedings of the DYMAT 2009—9th International Conferences on the Mechanical and Physical Behaviour of Materials under Dynamic Loading*; Brussels, Belgium, 7–11 December 2009, EDP Sciences: Les Ulis, France, 2009; Volume 1, pp. 511–516.
45. Walley, S.M.; Proud, W.G.; Rae, P.J.; Field, J.E. Comparison of two methods of measuring the rapid temperature rises in split Hopkinson bar specimens. *Rev. Sci. Instrum.* **2000**, *71*, 1766–1771. [[CrossRef](#)]
46. Romanova, V.; Balokhonov, R.; Panin, A.; Kazachenok, M.; Kozelskaya, A. Micro- and mesomechanical aspects of deformation-induced surface roughening in polycrystalline titanium. *Mater. Sci. Eng. A* **2017**, *697*, 248–258. [[CrossRef](#)]
47. Behera, A.K.; Ou, H. Effect of stress relieving heat treatment on surface topography and dimensional accuracy of incrementally formed grade 1 titanium sheet parts. *Int. J. Adv. Manuf. Technol.* **2016**, *87*, 3233–3248. [[CrossRef](#)]
48. Huang, W.; Zan, X.; Nie, X.; Gong, M.; Wang, Y.; Xia, Y. Experimental study on the dynamic tensile behavior of a poly-crystal pure titanium at elevated temperatures. *Mater. Sci. Eng. A* **2007**, *443*, 33–41. [[CrossRef](#)]
49. Bishoyi, B.D.; Sabat, R.K.; Sahu, J.; Sahoo, S.K. Effect of temperature on microstructure and texture evolution during uniaxial tension of commercially pure titanium. *Mater. Sci. Eng. A* **2017**, *703*, 399–412. [[CrossRef](#)]
50. Tsao, L.C.; Wu, H.Y.; Leong, J.C.; Fang, C.J. Flow stress behavior of commercial pure titanium sheet during warm tensile deformation. *Mater. Des.* **2012**, *34*, 179–184. [[CrossRef](#)]
51. Motyka, M.; Kubiak, K.; Sieniawski, J.; Ziaja, W. *Phase Transformations and Characterization of $\alpha + \beta$ Titanium Alloys*; Elsevier: Amsterdam, The Netherlands, 2014; Volume 2, ISBN 9780080965338.
52. Parker, R. *Rapid Phase Transformations in Titanium Induced by Pulse Heating*; Lawrence Radiation Lab, University of California: Livermore, CA, USA, 1964.
53. Cezairliyan, A.; Miiller, A.P. Thermodynamic study of the alpha beta phase transformation in titanium by a pulse heating method. *J. Res. Natl. Bur. Stand.* **1978**, *83*, 127. [[CrossRef](#)] [[PubMed](#)]
54. Kaschnitz, E.; Reiter, P. Enthalpy and Temperature of the Titanium Alpha-Beta. *Int. J. Thermophys.* **2002**, *23*, 1339–1345. [[CrossRef](#)]